

Geothermal state of the deep Western Alpine Molasse Basin, France-Switzerland



Cyril Chelle-Michou^{a,b,*}, Damien Do Couto^a, Andrea Moscariello^a, Philippe Renard^c, Elme Rusillon^a

^a University of Geneva, Department of Earth Sciences, 13 rue des Maraîchers, 1205 Geneva, Switzerland

^b Univ. Lyon, UJM-Saint-Etienne, UBP, CNRS, IRD, Laboratoire Magmas et Volcans UMR 6524, F-42023 Saint Etienne, France

^c University of Neuchâtel, Center for Hydrogeology and Geothermics (CHYN), 11 rue Emile Argand, 2000 Neuchâtel, Switzerland

ARTICLE INFO

Article history:

Received 17 December 2015

Received in revised form 19 October 2016

Accepted 13 January 2017

Keywords:

Geothermal anomaly

Geostatistics

Structure

Alpine Molasse Basin

Fluid circulations

Bottom hole temperature

ABSTRACT

Over the last few years the Western Alpine Molasse Basin (WAMB) has been attracting large institutional, industrial and scientific interest to evaluate the feasibility of geothermal energy production. However, the thermal state of the basin, which is instrumental to the development of such geothermal projects, has remained to date poorly known. Here, we compile and correct temperature measurements (mostly bottom hole temperature) from 26 existing well data mostly acquired during former hydrocarbon exploration in the basin. These data suggest that the average geothermal gradient of the WAMB is around 25–30 °C/km. We further use these data to build the first well data-driven 3D geostatistical temperature model of the whole basin and generate probabilistic maps of isotherms at 70 and 140 °C. This model highlights a number of positive and negative thermal anomalies that are interpreted in the context of heat advection caused by fluid circulation along faults and/or karst systems. This study confirms that the WAMB has a great potential for low-enthalpy geothermal resources and presents a typology of advection-dominated potential targets.

© 2017 Elsevier Ltd. All rights reserved.

1. Introduction

Over the last decades growing political, social and environmental concerns over energy consumption and future supply have stirred up the interest toward locally generated renewable and alternative sources of energy. In this context, several projects aiming at assessing the geothermal potential of previously overlooked basins have originated. As part of this effort, the European Community recently sponsored projects focusing either on specific geographical areas such as the Alpine foreland basins (e.g., [GeoMol Team, 2015; Lo Russo et al., 2009](#)) or the development of advanced exploration methods (IMAGE Project, <http://www.image-fp7.eu>) dedicated to geothermal exploration.

These areas (such as the Molasse Basin) are devoid of magmatic activity and are potentially associated with low-enthalpy geothermal resources with a maximal temperature of less than 150–200 °C. Such geothermal systems are typically characterized by the absence of steam (i.e. only water), by formation temperatures close to nor-

mal geothermal gradients (25–50 °C/km), by maximal depth of 3000–5000 m and by vertical heat conduction and/or advection in fractured or highly permeable stratigraphic units. Current technological capabilities (e.g., binary plant technology) allow direct-use of the geothermal energy from low-enthalpy resources and even electric power production for the highest temperatures (>80 °C; e.g., [Bertani, 2012; DiPippo, 2004](#)).

In the Western Alpine Molasse Basin (WAMB; [Fig. 1](#)), several ongoing geothermal projects aim at exploring the potential of deep aquifers (>1500 m depth) in the thick Phanerozoic sedimentary succession, which locally may attain up to 5000 m in thickness. In this area, more specifically in Switzerland, important exploration projects (GEothermie 2020 in the Canton of Geneva, Lavey-les-Bains and La Côte in the Canton of Vaud, etc.) and national academic research programs (SCCER-SoE, <http://www.sccer-soe.ch>) are being strongly supported both by industry and governments in order to meet both economic and long term energy strategy goals (Europe 2020 targets, <http://ec.europa.eu/europe2020/targets/eu-targets/>).

From a geological perspective, favorable sites for the development of long-term economic geothermal resources require the presence of a (1) large amount of fluids hosted in a (2) permeable rock formation (through porosity or fractures) at a (3) sufficiently

* Corresponding author at: School of Earth Sciences, University of Bristol, Wills Memorial Building, Queens Road, Bristol BS8 1RJ, UK.

E-mail address: cyril.chelle-michou@bristol.ac.uk (C. Chelle-Michou).

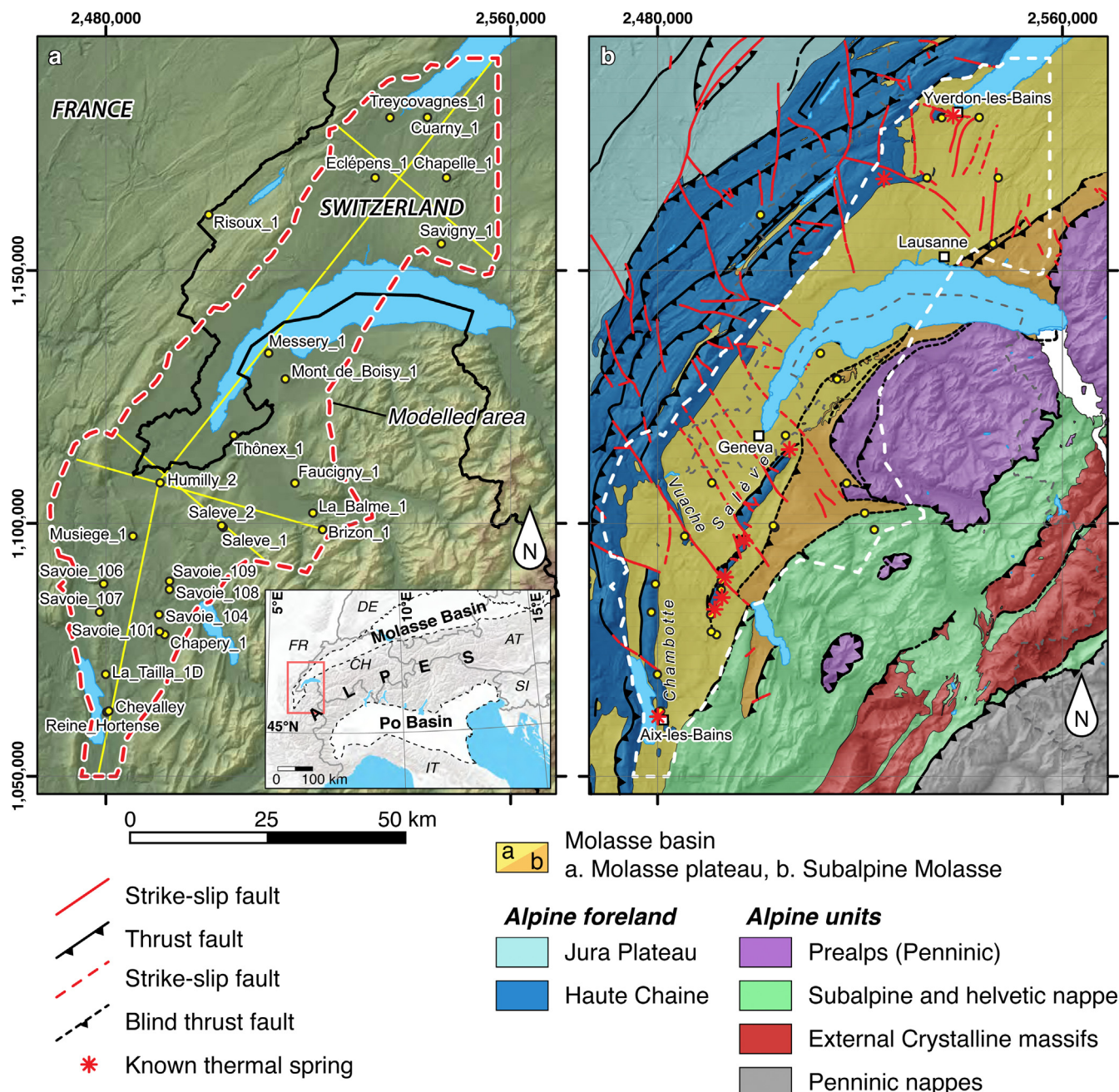


Fig. 1. Map of the WAMB. (a) location of the study area and of the wells used for the modelling. The yellow lines indicate the location of the cross sections shown in Figs. 9–11. (b) Tectonic map of the WAMB. (For interpretation of the references to color in this figure legend, the reader is referred to the web version of this article.)

high temperature (at least 50–70 °C). Predictive models of subsurface formation temperatures are therefore instrumental to develop effectively these projects and to manage the associated potential risks and uncertainties as well as to the determination of key thermal parameters (geothermal gradient, heat flow and available heat) which may determine the success of a geothermal exploitation. Furthermore, local perturbations of the geothermal gradient may reveal zones of fluid circulation and thereof zones of enhanced permeability.

Temperature data throughout the deep WAMB have been acquired over successive hydrocarbon exploration campaigns carried out since the 1930s until the 1990s as well as from few younger geothermal wells. While some of these data have been used in technical reports assessing the geothermal potential of the area, an integrative data-driven thermal model of the WAMB is necessary in

order to maximize the value of these data and thus provide preliminary guidelines for geothermal exploration in this region. In this paper, we present the results of the compilation, processing and re-interpretation of available temperature data from several wells penetrating the deep WAMB (>500 m depth) and the outcomes of the first 3D geostatistical thermal model of the entire basin as well as the computed probability maps of the isotherms of interest.

2. Geological setting

The WAMB forms the westernmost termination of the wider North Alpine Foreland Basin that extends parallel to the Alpine orogen from France to Austria (see inset Fig. 1, Kuhlemann and Kempf, 2002). It results from the collision between the European and the Adriatic-African plates during the Alpine orogeny (Pfiffner,

1986). This area is usually known as the Molasse Basin in reference to the Oligocene–Miocene siliciclastic deposits covering a Mesozoic and Paleozoic sedimentary succession. The study area extends from Yverdon-les-Bains to Aix-les-Bains (from north to south) and is limited to the NW by the Jura Mountains and to the SE by the thrusting front of the Alpine units (Fig. 1).

The WAMB is a typical asymmetric foreland basin (Sommaruga et al., 2012) characterized by a NW erosional border on the Jura and a thrusted SE border hidden under the Alpine nappes. The Jura is an arcuate fold belt divided into sub-domains depending on their tectonic styles: the External Jura made of relatively flat areas called Plateau and the Internal Jura (also referred as the Haute Chaine; Fig. 1). The Alpine units are divided from the NW to the SE in the Prealps klippe, the Subalpine and Helvetic nappes including the External Crystalline Massifs and the Penninic nappes (Fig. 1).

The Molasse Basin consists of a thick Mesozoic and Cenozoic sedimentary cover (3000–5000 m of sediments) which overlays the Variscan crystalline basement gently dipping to the S-SE (1° – 3°). The oldest units do not crop out in the basin but have been drilled by several wells (Fig. 1) and are well-described in the literature (Charollais et al., 2007; Gorin et al., 1993; Signer and Gorin, 1995; Sommaruga et al., 2012). Above the crystalline basement, the stratigraphic succession composing the WAMB extends from the Late Carboniferous to Quaternary (Fig. 2). Stratigraphic units described hereafter according to the International Stratigraphic Chart (Cohen et al., 2013) are also named according to their German terminology. The stratigraphic units can be summarized from bottom to top as follows:

- Late Carboniferous and Permian clastics sediments were deposited in SW-NE oriented grabens and relatively small confined basins, related to the collapse of the Variscan orogeny (McCann et al., 2006; Wilson et al., 2004).
- The Triassic period is marked by the deposition of shallow marine sediments in an epicontinent sea environment. The Lower Triassic (Buntsandstein in the German terminology) is characterized by the deposition of sandstone. It is overlain by Middle Triassic carbonates and dolomites (Muschelkalk) and a thick sequence of evaporites (Keuper).
- The deposition of marls and shales during the Lower Jurassic (Lias) evolves to alternating limestones and carbonaceous shales with local patch reefs from the Middle to Upper Jurassic (Dogger and Malm).
- The Lower Cretaceous is marked by shallow water carbonate platform deposits with bioclastic limestone, whereas the Upper Cretaceous is missing. A major subaerial erosional surface affects the top of the Lower Cretaceous, and is associated with the development of karsts, filled by oxidized continental deposits attributed to the Late Eocene.
- Oligocene to Late Miocene siliciclastic deposits, of marine and continental environment, form the Molasse wedge above the Mesozoic series. The Subalpine Molasse, involved in a series of imbricated thrust sheets, is composed of clastic sandstone and marls originated in either marine or continental freshwater depositional environment, while the rest of the Molasse (Molasse plateau in Fig. 1) mostly consists of clastic sediments of continental origin.

The structural pattern of the WAMB is characterized by two major groups of faults. The most striking structures are SW-NE trending thrusts delineating the southeastern rim of the basin (Alpine front thrust), associated thrusts in the subalpine Molasse, and a series of thrusts in the Haute-Chaine of the Jura (including along the Salève and the Chambotte ridges). In addition, several strike-slip (or wrench) faults systems, mostly with sinistral movement, cross the basin off-setting some of the thrust faults (Fig. 1b).

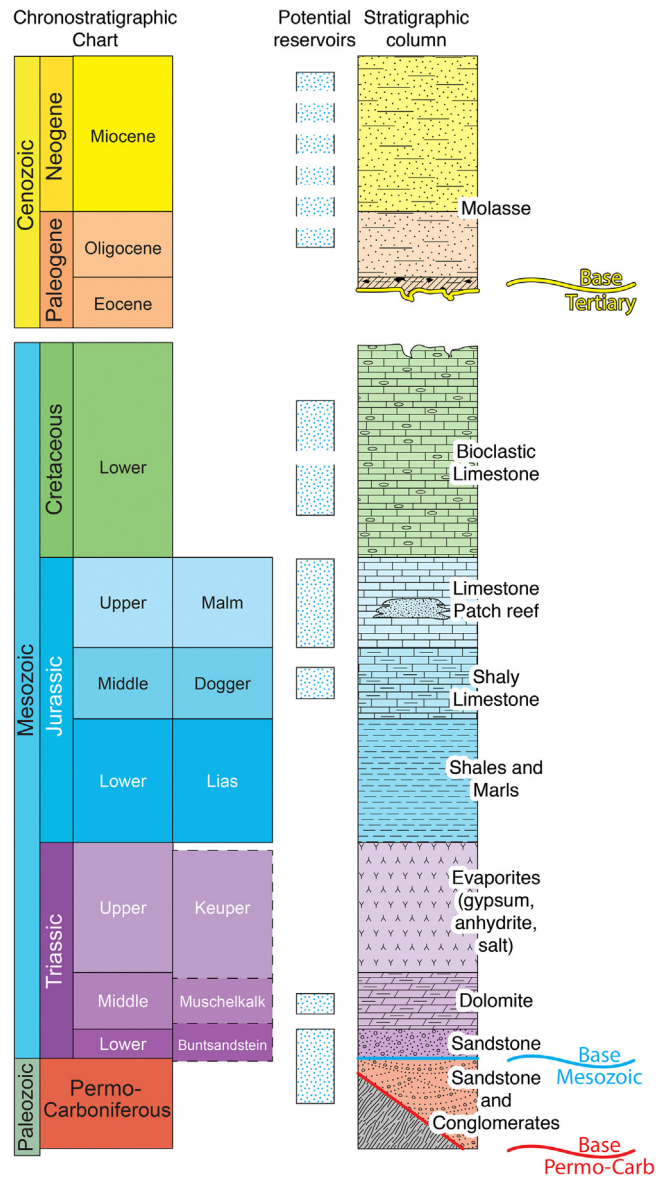


Fig. 2. Synthetic log of the stratigraphy and possible reservoirs of the WAMB (based on Rybach, 1992; Chevalier et al., 2010).

These structures, locally outcropping at the surface (e.g. the Vuache Mountain) are mostly oriented NW-SE. In addition, late Alpine tectonics resulted in the development of SW-NE trending, low-relief, anticlinal and synclinal flexures in the Cenozoic and Mesozoic sequence (Signer and Gorin, 1995) as well as few thrust ridges (e.g. the Salève and Chambotte ridges; Fig. 1b). At depth, the Triassic evaporitic unit made of salt and gypsum/anhydrite serves as a major décollement layer accommodating the compressional deformation of the Alpine foreland (Sommaruga, 1999). The décollement of the Mesozoic and Cenozoic strata over the Permocarboniferous troughs and Paleozoic basement extends under the Jura Mountains making the Molasse Basin a piggyback basin (Willett and Schlunegger, 2010).

Over the past few years, a series of potential aquifers have been identified in the stratigraphic series of the Molasse Basin (Baujard et al., 2007; Chevalier et al., 2010; Rybach, 1992). From the bottom to the top they consist of the Permocarboniferous and Lower Triassic sandstones (Bundsandstein), the Middle Triassic carbonate (dolomite of the Muschelkalk), the Upper Jurassic limestone

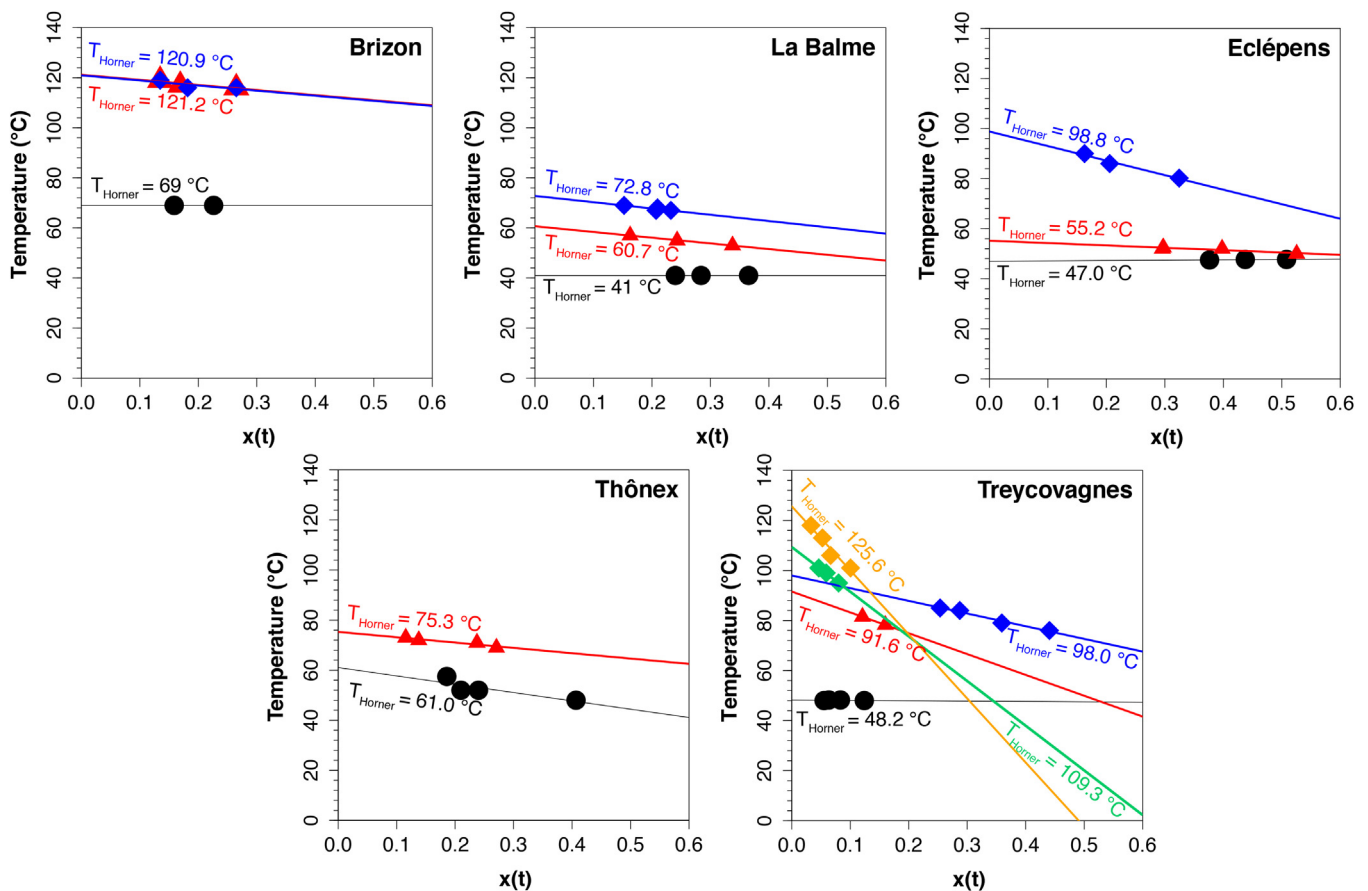


Fig. 3. Horner plots for the five wells where successive measurements at the same depth together with full measurement history have been reported.

(including patch reef of the Malm), and the freshwater Molasse sandstone (Fig. 2).

3. Data compilation and correction

3.1. Available data

Temperature data in the WAMB were compiled from available down hole logging headers and well reports. As we focus on the deep part of the basin, only wells deeper than 500 m were considered (Fig. 1a). In total we gathered 170 temperature measurements from 26 drill holes (7 in Switzerland, 19 in France), among which 145 are Bottom Hole Temperature (BHT) measurements and 25 are Drill Stem Test (DST), emergence or equilibrium temperature. The stratigraphic unit at measurement depth were also compiled from the well reports and the French geological survey (BRGM) validated database (<http://infoterre.brgm.fr>). All the wells (except Thôñex and La Tailla 1D) are vertical and in the absence of detailed deviation measurements, the drilled length is assumed to be equal to the vertical depth.

It is noteworthy that, in most drill holes, several BHTs have been measured at the same depth, which overall diminishes the depth continuity of the thermal record. In most cases the respective time of the measurements and the duration of the mud circulation had not been reported. Fortunately, successive BHT measurements at the same well depth, but at different shut-in-time, with fully documented measurement history are available for 5 drill holes: Eclépens (Switzerland), Thôñex (Switzerland), Treycovagnes (Switzerland), Brizon (France) and La Balme (France).

3.2. Selection of a BHT correction method

BHT data are usually collected during the down hole logging phase that follows drilling by few hours. During the drilling operations, the circulation of the drilling mud causes transient thermal disturbance in the surrounding rocks, which results in the BHT being typically lower than the true static formation temperature. It results that, as opposed to DST, emergence or equilibrium temperature (collectively referred to as ‘formation temperatures’) that do not require any correction, raw BHT data need to be corrected in order to recover the static formation temperature of interest (Deming, 1989; Nielsen et al., 1990). Several correction methods have been proposed and rely on a detailed knowledge of the measurement history, of the borehole geometry, of the thermal properties of the surrounding rocks, and/or of the thermal properties of the mud (see review in Goutorbe et al., 2007; Pasquale et al., 2008; Wong-Loya et al., 2015). The most precise and accurate corrections methods logically require a maximum of information about the measurement history and conditions, which is often critically lacking in old logging headers where the BHTs are reported. Alternatively, less precise but overall fairly accurate empirical corrections have been calibrated on mature oil fields where a large number of both accurate formation temperatures and BHTs are available (e.g., Deming, 1989; Forster and Merriam, 1995; Forster et al., 1997; Harrison et al., 1983; Lucazeau and Ben Dhia, 2011; Pasquale et al., 2012). Given the age of the wells and the lack of precise information, these empirical corrections are best suited for the correction of BHT recovered in the study area.

In order to select the most appropriate empirical correction method for the WAMB, we propose to compare them to the well-established analytical Horner correction method (Dowdle and

Cobb, 1975; Horner, 1951) for the five drill holes (Treycovagnes, Eclépens, Thônex, La Balme and Brizon; Fig. 1) where measurement times have been reported. The Horner correction requires the knowledge of the circulation time before shut-in (t_c), and the time elapsed since circulation stopped for each successive BHT measurement at a given depth (t). Despite the fact that this method is widely used and is generally accurate, it has been shown to return temperature that might be slightly lower (by no more than 5% relative) compared to the “true” static formation temperature, especially for short elapsed time and/or for large hole radii (Forster, 2001; Goutorbe et al., 2007). However, in the present case, the available information limits the comparison to another potentially more accurate methods (e.g. cylindrical heat source method). The Horner equation is classically expressed in a linear form as:

$$BHT(t) = T_{Horner} + m_{Horner}x(t) \quad (1)$$

where T_{Horner} is the corrected temperature, m_{Horner} is the slope of the linear regression through the data and $x(t)$ is the dimensionless Horner time function expressed as:

$$x(t) = \log\left(\frac{t_c + t}{t}\right) \quad (2)$$

The Horner-corrected temperatures for the five wells range from 41 °C to 125.6 °C at depth of 854 m and 3210 m, respectively, and encompass most of the temperature-depth range investigated in the present study (Fig. 3).

Empirical BHT corrections are typically expressed in the form of polynomial equations as a function of depth. Here, we consider two of the most used formulations that have been calibrated in American basins. The formulation of Deming (1989) has been calibrated in Texas and Louisiana and is expressed as:

$$\begin{aligned} T_{corr} = & T_{BHT} + 1.878 \cdot 10^{-3} z + 8.476 \cdot 10^{-7} z^2 \\ & - 5.091 \cdot 10^{-11} z^3 - 1.681 \cdot 10^{-14} z^4 \end{aligned} \quad (3)$$

where T_{corr} is the corrected BHT in °C, T_{BHT} is the measured BHT in °C and z is the depth of measurement in m. The formulation of Harrison et al. (1983) has been calibrated in Oklahoma and is expressed as:

$$T_{corr} = T_{BHT} - 16.51 + 0.01827 z - 2.345 \cdot 10^{-6} z^2 \quad (4)$$

Note that in both cases, successive measurements at a given depth will be affected by the same correction, however, they will return the same temperature only if their BHT is already similar. Both empirical corrections were applied to all BHTs from the five reference wells and yield corrected temperatures similar to those obtained with the Horner correction (Fig. 4). However, relative to the Horner correction, the Harrison correction returns more dispersed data than the Deming correction. Indeed, the determination coefficient (r^2) to a 1:1 relation between the Horner and Harrison methods is 0.91, while it yields 0.95 when compared to the one of Deming (Fig. 4). This shows that the empirical correction of Deming (1989) yields the most similar results to the Horner method, and that it might be the most appropriate of the two to correct BHTs from the WAMB (where no more information than the BHT are available). The average absolute difference between the Horner- and Deming-corrected temperatures is 4.8 °C (with a maximum of 13.9 °C) and can be used as a proxy for the uncertainty (1σ) associated with the Deming correction method on BHTs from the WAMB. Such uncertainty is typical of those associated with corrected BHT data (Andaverde and Verma, 2005; Goutorbe et al., 2007).

In the light of this analysis, all the BHTs from the WAMB were corrected with the Deming empirical correction. A fixed uncertainty of 5.25 °C has been considered for each corrected BHT and corresponds to the quadratic addition of the uncertainty associated with the Deming correction and an additional arbitrary 0.5 °C

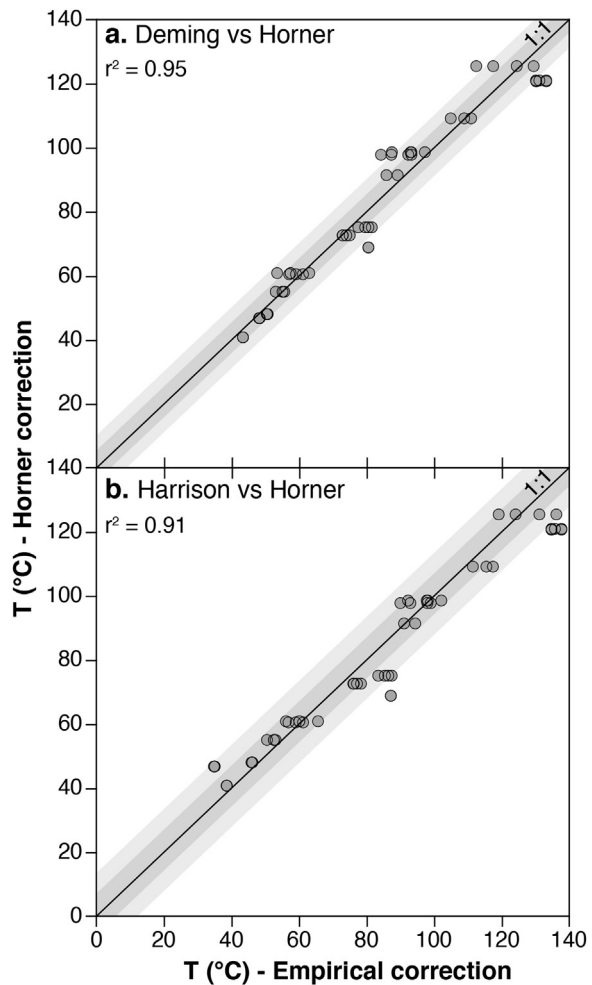


Fig. 4. Comparison between the Horner correction and (a) the Deming (1989) or (b) Harrison et al. (1983) empirical correction methods. Shaded grey areas correspond to once and twice the average difference between the Horner and the corresponding empirical correction.

uncertainty corresponding to the measurement error. Uncertainties of the 25 formation temperatures therefore only include the one associated with the measurement (± 0.5 °C). In case several temperature data were available for the same depth we have computed the average of the corrected BHTs or of the formation temperatures, accordingly. In total, we end up with a dataset of 126 temperature data for the WAMB (Fig. 5a).

4. Geothermal gradient(s) and heat flow

4.1. What is the average thermal gradient of the WAMB?

The geothermal gradient describes the evolution of the temperature with depth. It is usually assumed to be linear and to show limited depth-dependent variations in the upper crust. However, in detail, the contrasted thermal conductivity of different formations in a sedimentary section (conductive heat refraction), as well as fluid migration (convection) can locally deflect the gradient.

With an imposed mean annual surface temperature of 10 °C (Geneva average, www.meteosuisse.ch), the linear least-square fitting to the corrected temperature versus depth data yield an average geothermal gradient of 30.1 °C/km ($r^2 = 0.86$; dashed blue line on Fig. 5). We notice that at shallow depth (<1000 m) nearly all of the data points lie above this geotherm. In case surface temperature is not assigned, the linear least-square best fit to the corrected data

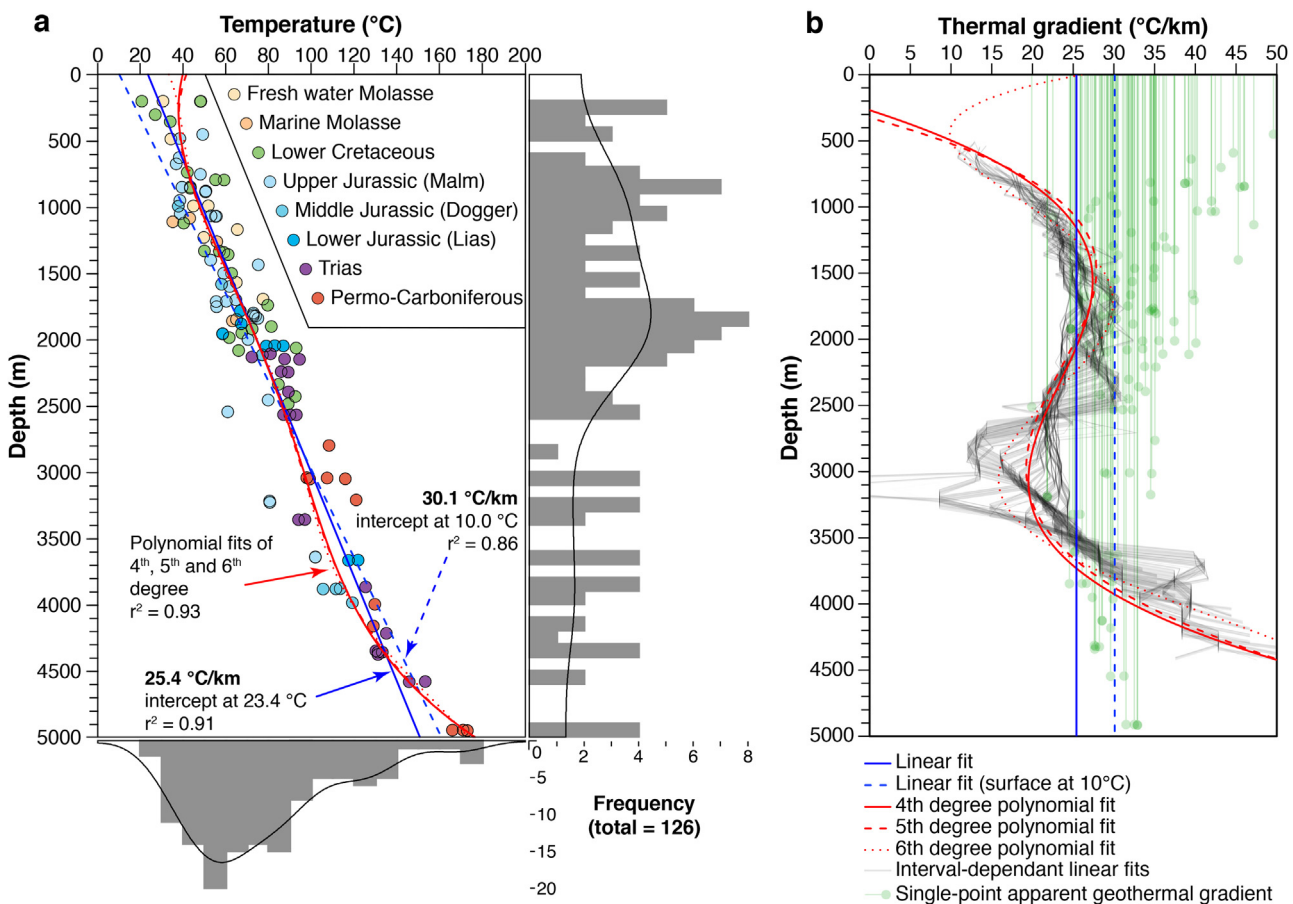


Fig. 5. (a) Formation temperatures and corrected BHTs versus depth data for the WAMB with several fitting geotherms. (b) depth dependence of the geothermal gradient of the WAMB using different calculation methods (see text for details).

yield an average gradient of 25.4 °C/km with a surface intercept at 23.2 °C ($r^2 = 0.91$; solid blue line on Fig. 5).

Considering only points below 2000 m depth, the linear fitting yields a gradient of 26.6 °C/km (not represented in Fig. 5), which is very similar to the one determined for the whole dataset. In turn, when considering data from the upper 1500 m, the average gradient is of 17.4 °C/km. This shows (1) that the temperature gradient in the WAMB is not linear (i.e. vary with depth), and (2) that the calculation of the gradient based on a linear least-square fitting may strongly depend on the selection of the depth interval used to compute it. To illustrate the first phenomenon, we computed thermal gradients as the derivative of 4th to 6th degree polynomial least-square fittings to the corrected data (red lines on Fig. 5). These result in only minor improvement of the regression statistics ($r^2 = 0.93$) and show that the linear fitting is an overall good description of the data through the basin. To illustrate the second phenomenon, we computed the thermal gradient obtained by linear least-square fitting on a fixed interval length moving from top to bottom by steps of 100 m. The resulting gradients were assigned to the central depths of the intervals, and the resulting gradient-depth profile was plotted on Fig. 5b (individual grey lines). For example, with an interval length of 1200 m, the gradient in the 0–1200 m depth interval was plotted at 600 m depth, then the gradient in the 100–1300 m interval depth was plotted at 700 m depth, and so on until the entire profile is constructed. We ran this process 2000 times by randomly varying the interval length between 1000 and 3000 m. In Fig. 5b, the darkest areas represent the highest density of grey lines. In all cases (polynomial gradient or interval-dependent linear gradients)

we observe a clear increase (from ~10 °C/km to 25–30 °C/km) of the geothermal gradient from 500 to 1500 m depth. The slight gradient decrease between 2000 and 3000 m depth is likely an artefact resulting from the very low amount of data within this interval (see frequency diagram in Fig. 5a). Despite the deepest part of the basin (>3000 m) is constrained by only few points, we also notice a clear increase (from ~20 °C/km to >50 °C/km) in the thermal gradient from 3000 m to 4500 m depth (Fig. 5b).

Previous geothermal gradient estimates in the WAMB range from 30 to 40 °C/km (Jenny et al., 1995; PGG, 2011; PGV, 2003; Rybach, 1992; SIG, 2011). These anomalously high gradients were determined for individual wells on the basis of only few (often only one) temperature measurements with an imposed surface temperature of 10 °C. Using a similar approach, we calculated the apparent thermal gradient for each data point (as $(T-10)/z$; green lines on Fig. 5b). We obtain a mean gradient at 38.3 °C/km (median at 32.3 °C/km). Strikingly, linear regressions through our dataset result in significantly lower gradients of 25.4–30.1 °C/km (depending on imposing a surface temperature or not). This analysis shows that data point-specific gradients are unlikely to capture the average depth-temperature dependency of the WAMB. Instead, a regression analysis through all the available data provides a far more accurate and mathematically more correct description of the average thermal state of the basin. It is noteworthy that the average geothermal gradient we have obtained for the WAMB compares well with the rest of the North Alpine Molasse basin (Agemar et al., 2012; GeoMol Team, 2015), of the Po basin (Pasquale et al., 2012, 2008) and of foreland basins in general (Allen and Allen, 2013).

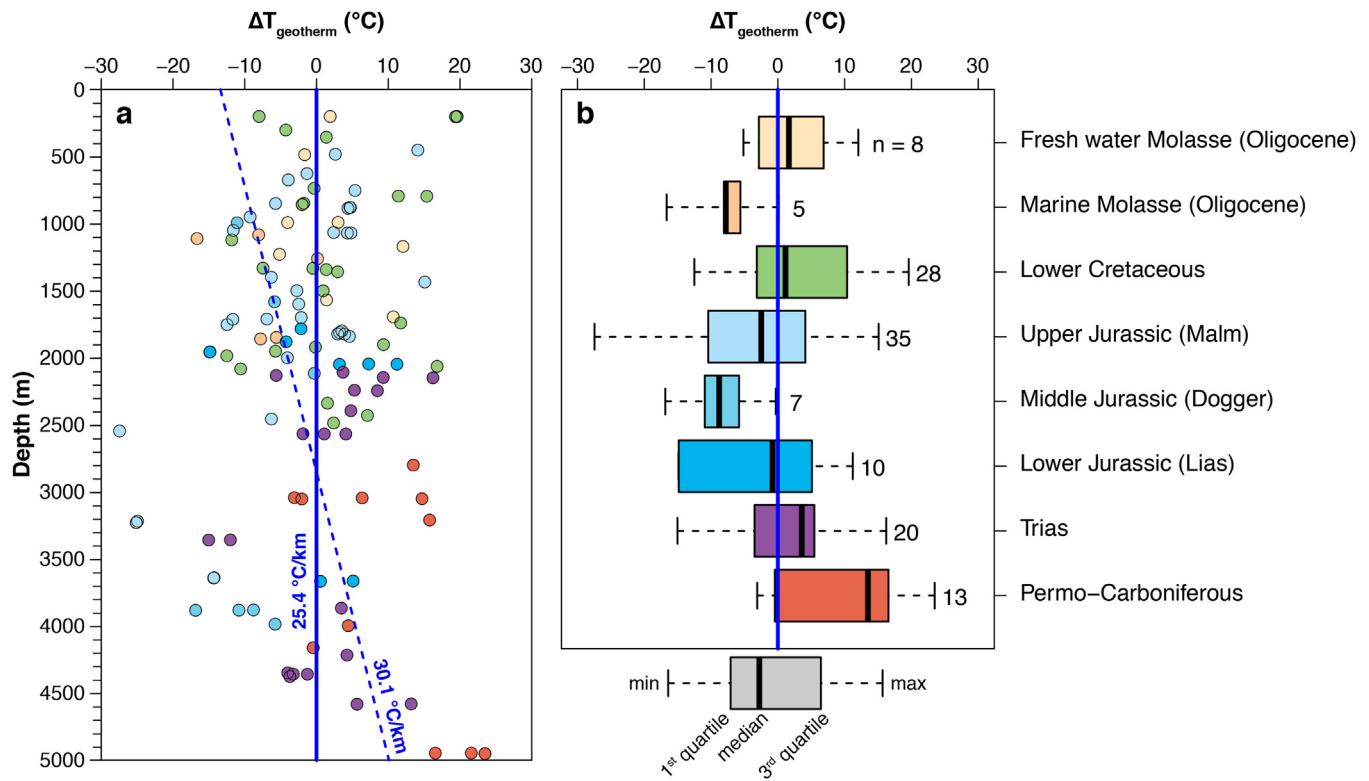


Fig. 6. Residual temperatures compared to the best linear gradient of the data with free surface intercept (a) versus depth, and (b) versus stratigraphic unit.

4.2. Heat flow

The averaged heat flow in the WAMB can be calculated as:

$$Q = K \cdot \frac{\partial T}{\partial z} \quad (5)$$

where $\frac{\partial T}{\partial z}$ is the geothermal gradient and K in the thermal conductivity of the rocks. Considering an average thermal gradient of $25.4\text{--}30.1 \text{ }^{\circ}\text{C}/\text{km}$ for the WAMB, and that the bulk thermal conductivity of the sedimentary pile lies within 2.5 and 2.7 W/m/K , this corresponds to an average heat flow of $64\text{--}82 \text{ mW/m}^2$ for the basin. These values are similar to previous estimates of the crustal

heat flow in western Switzerland presented by [Medici and Rybach \(1995\)](#).

5. 3D geostatistical thermal bloc model

5.1. Pre-processing of the dataset

A 3D thermal model for the WAMB has been computed by geostatistical interpolation of the corrected temperature data presented above while also considering their assigned uncertainties. We used kriging since it is an approach that allows to interpolate rock properties (e.g. ore grade, porosity, ...) while honoring precisely the data (exact interpolator), correcting for spatial clustering of the input data, and, even more interestingly, quantifying

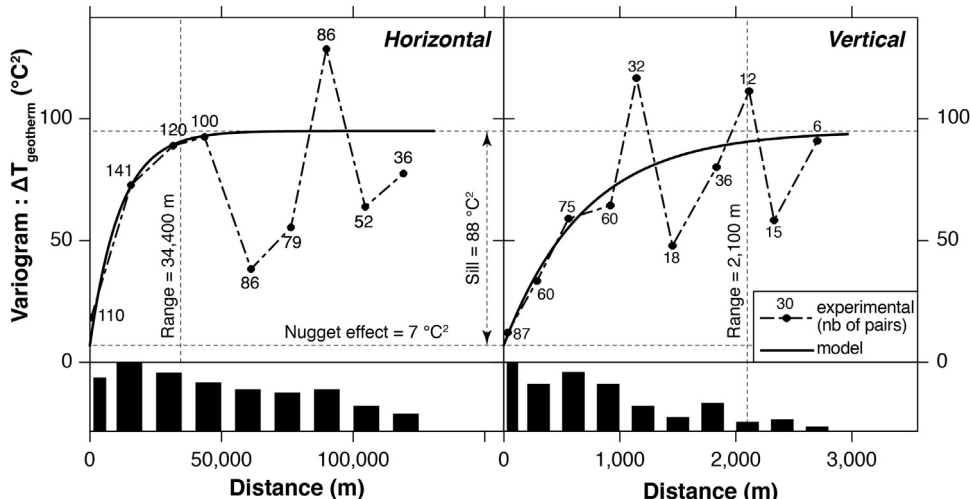


Fig. 7. Experimental and model variogram for the residual temperatures (see text for details).

uncertainties in the estimated values (Chilès and Delfiner, 2012). Because the temperature distribution in the WAMB increases with depth (Fig. 5a) we used simple kriging with a local mean. As compared to other methods that account for trends (such as kriging with an external drift or collocated cokriging), it is simple to apply and pretty reliable (Goovaerts, 2000). This method has also been applied previously for 3D thermal fields (e.g., Agemar et al., 2012; Garibaldi et al., 2010; Guillou-Frottier et al., 2013; Rühaak, 2014; Sepúlveda et al., 2012; Teng and Koike, 2007). Here, the average geothermal gradient was used to estimate the local mean. The method requires then to analyze the residual temperature $\Delta T_{\text{geotherm}}$, which, by construction, can be reasonably assumed to be a stationary property with a zero mean (Fig. 6a):

$$\Delta T_{\text{geotherm}}(x, y, z) = T(x, y, z) - T_{\text{geotherm}}(z) \quad (6)$$

where $T(x, y, z)$ is the temperature data (corrected BHT or formation temperature) and $T_{\text{geotherm}}(z)$ is the temperature of the average geotherm at the same depth. We used the linear geotherm with no imposed surface temperature to ensure the stationarity of the interpolated variable (i.e. $T_{\text{geotherm}}(^{\circ}\text{C}) = 25.4 \times z(\text{km}) + 23.2$). Indeed, we cannot fix the surface temperature at 10°C otherwise the residual temperature ($\Delta T_{\text{geotherm}}$) would show a tendency of decreasing with increasing depth (especially for the first 2000 m; Fig. 6a) and the hypothesis of stationarity would not be satisfied. Because the study area presents some topographic relief (Fig. 1), all the vertical depth (z) of the residual temperature were converted into absolute altitude coordinates (z^*) above sea level.

Subsequently, we used the Isatis® software (Geovariances) to geostatistically analyze the data (variographic analysis) and to estimate a 3D thermal bloc model for the WAMB using kriging.

5.2. Variogram inference

In order to describe the spatial correlation of the residual temperatures, we computed the experimental variogram of the data. For a given distance (h) between data point pairs, the variogram value ($\gamma(h)$) is defined as the half mean square of the differences between pairs of measured value of inter-distance h (Chilès and Delfiner, 2012):

$$\gamma(h) = \frac{1}{2} \frac{\sum_{i=1}^{N(h)} [\Delta T_{\text{geotherm}}(x_i) - \Delta T_{\text{geotherm}}(x_i + h)]^2}{N(h)} \quad (7)$$

where $\Delta T_{\text{geotherm}}(x_i)$ denotes a measured value at the location x_i (in (x, y, z^*) coordinates) and $N(h)$ is the number of pairs of observation distant by h (in 3D).

We computed variograms in the horizontal (x, y) and vertical directions (z^* , Fig. 7). These two directions are considered the most relevant in our case because the residual temperature is mostly controlled by rock properties (e.g. thermal conductivity, permeability, etc) that are distributed subhorizontally according to the stratigraphy, and by the structures that are essentially subvertical (wrench faults) or subhorizontal (décollement). We used a slicing height of 200 m for the horizontal direction and a lag distance of 15 km. The vertical variogram was computed with a vertical angle tolerance of 30° and a lag distance of 300 m. These parameters ensure that most lag interval contains a statistically significant number of pairs (>30 pairs, Olea, 1999). As expected, the experimental variograms show a strong anisotropy of the residual temperatures between the horizontal and the vertical directions (Fig. 7).

The experimental variogram was fitted with a variogram model including a nugget effect of 7°C^2 , and an exponential model with a sill of 88°C^2 (above the nugget effect), a horizontal range of 34,400 m, and a vertical range of 2,100 m (Fig. 7). The nugget corresponds to the very short distance variability (it could be related to some noise in the data), the range can be interpreted roughly as

the distance over which the data are no longer correlated, and the sill represent the variance of the random field over the range.

The quality of the variogram was then checked with the Isatis® built-in cross-validation method where the residual temperature (and its variance) of each point of the dataset is estimated based on all the other data points. The cross-validation procedure yields a variance normalized error (mean difference between the estimated and the input residual temperatures divided by the kriging variance) of 0.001 indicating that there is no bias in the estimation (the mean error is zero). The standard deviation of the errors is equal to 0.947 indicating that the estimated order of magnitude of the errors (kriging variance) corresponds well with the predictions. Finally, a correlation coefficient of 0.838 indicates a pretty good correlation between the estimated values and the true values. We also noted that no correlation exists between errors and the values ($r = -0.06$, where r is the linear correlation coefficient). These relatively good statistics together with the small size of the dataset (126 points) does not justify the use of more complex structures for the variogram model.

5.3. 3D estimation

The residual temperature was interpolated with simple kriging over the entire basin meshed to 500 m (x) \times 500 m (y) \times 10 m (z^*) grid elements using the model variograms defined previously (Fig. 8). In order, to compute the temperature in each point of this grid, the interpolated residual temperature need to be added to the reference linear geotherm computed at the same depth (z). The altitude to depth transformation was based on a smoothed digital elevation model (DEM) of the study area. The smoothing of the DEM was done by a moving average procedure for an arbitrary diameter of 3000 m around each point. This procedure ensures that small scale topographic variations do not strongly affect the computed temperature field at depth. However, we note that a more rigorous approach would require to consider an increasingly smoothed topography with increasing depth. It results that while the uncertainty of interpolated residual temperature is directly provided by the kriging procedure, an additional uncertainty due to the arbitrary topographic smoothing would need to be considered when interpreting the temperature field. Nevertheless, because the topography in the study area is overall rather smooth, except for some relatively small ridges in the southern part (Vuache, Salève, Chambotte; Fig. 1), this uncertainty is considered to be mostly negligible.

The 3D temperature model is shown in Fig. 8 and selected cross-sections are presented in Figs. 9–11. We stress that the cross-validation test shows that the estimated residual temperatures and variance fields are accurate description of the temperature field of the basin.

5.4. Isothermal probability fields

One advantage of the uncertainty estimations provided by the kriging procedure is that they can be used to make a probabilistic assessment of the thermal field on the WAMB. Instead of providing only the mean (most probable) temperature at a certain location, we also estimated in each location the probability that the temperature could be above 70°C and 140°C (Fig. 12). These isotherms were selected because they correspond to the targeted temperatures of the GEothermie 2020 program (www.geothermie2020.ch) in the deep Geneva basin. This calculation is based on the assumption that the estimates are normally distributed around the kriging values and that the variance around this mean is given by the kriging variance. Based on this assumption one can compute in any point of the domain the probability $P_{T_{\text{iso}}}(x, y, z^*) = P[T(x, y, z^*) > T_{\text{iso}}]$

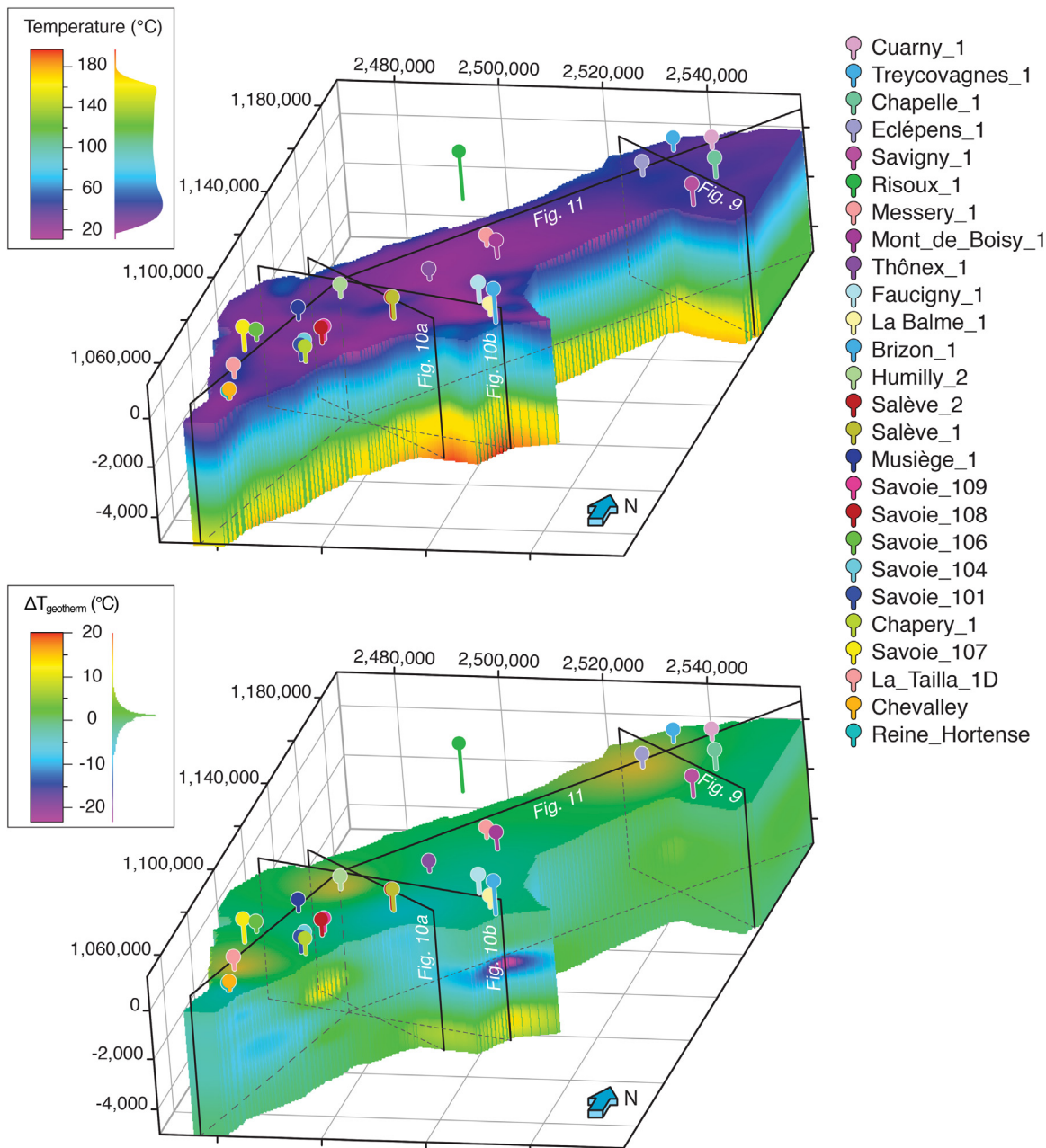


Fig. 8. Geostatistical 3D thermal model of the WAMB displayed in term of temperature (top) and residual temperature (compared to the linear best fit gradient; bottom).

that the (true and unknown) temperature is higher than a given temperature T_{iso} :

$$P_{T_{\text{iso}}} (x, y, z^*) = 1 - \Phi \left(\frac{T_{\text{iso}} - T_{\text{interp}}(x, y, z^*)}{\sigma_{\text{interp}}(x, y, z^*)} \right) \quad (8)$$

where Φ is the standard Gaussian cumulative distribution function, $T_{\text{interp}}(x, y, z^*)$ and $\sigma_{\text{interp}}(x, y, z^*)$ are the temperature and kriging variance derived from the 3D geostatistical model, respectively. For each isotherm, the probability field contains values between 0 (toward the top) and 1 (toward the base) describing the degree of confidence in the computed temperature of interest. Logically, the probability field widens away from the data points and becomes narrower close to them. We emphasize that the computed surfaces (Fig. 12) do not represent the best fit isotherms neither the true surfaces of the isotherms, but rather the surfaces below which there is 95% of chances that the 70 °C and 140 °C temperatures are

exceeded. Therefore, it incorporates a measure of the risks associated with the temperature estimate.

6. Large scale thermal anomalies in the WAMB

6.1. High temperatures at shallow depth

On average, temperatures for the first 2000 m below surface do not converge to the expected 10 °C on surface and tend to be higher than expected while defining a low geothermal gradient increasing with depth (Fig. 5). This has also been noted in a number of studies (e.g., Bonte et al., 2010; Davis, 2012; Forster and Merriam, 1995; Gray et al., 2012; Guillou-Frottier et al., 2013). Several factors may account for these anomalous temperatures: (1) recent "instantaneous" erosion of few hundreds of meters (see Allen and Allen, 2013); (2) inaccurate BHT correction at shallow depth; (3) use of maximum temperature thermometers during summer months

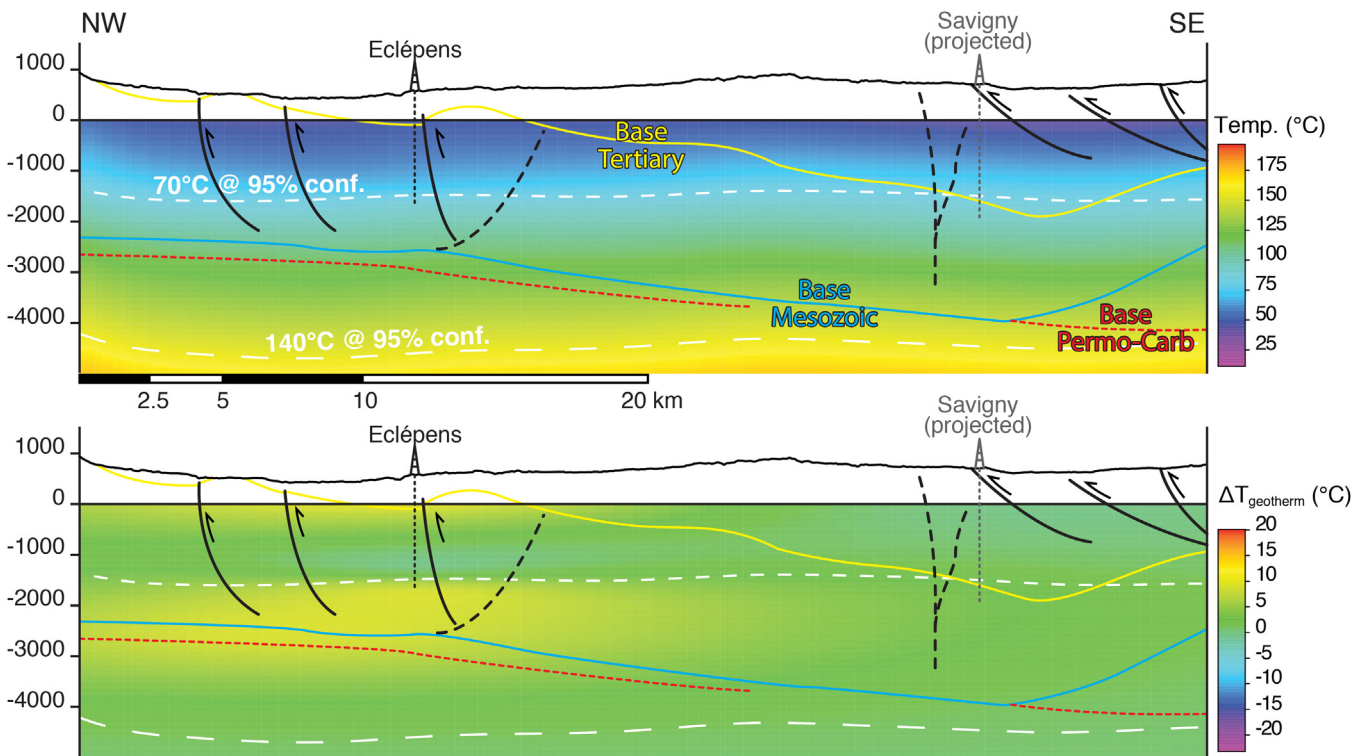


Fig. 9. NW-SE cross section in the 3D model for the northern part of the WAMB. The exact location of the section is shown on Figs. 1 and 8. Geological interpretation are from Gorin et al. (1993) and Sommaruga et al. (2012). Note that the thickness of the Permo-Carboniferous unit remains poorly constrained and is hence displayed as a red-dashed line.

(e.g., Gray et al., 2012); (4) thermal blanketing by poorly conductive near-surface sediments (Quaternary moraine, Molasse); (5) dataset biased by an excessive number of measurements in discharging hydrothermal systems.

Hypothesis (1) can readily be excluded because the last period of intense erosion dates back to at least 4 Ma (Cederbom et al., 2004, 2011; Hage et al., 2012), which would have left more than enough time for the basin to come back to thermal equilibrium.

The BHT correction method we have used assumes that the measured BHT is cooler than the formation temperature. Several authors have argued that while mud circulation drives transient cooling of the deep subsurface, it can also drive heating at shallower depth (Bonte et al., 2010; Forster, 2001; Pasquale et al., 2012). However, when temperature measurements have been done successively at the same depth within the shallowest 2000 m, progressive cooling has never been observed (Fig. 3). This suggests that hypothesis (2) is likely to be rejected and that the assumption that BHTs are cooler than the formation temperature is mostly valid in our case.

Before the years 2000, BHT measurements were mostly conducted with maximum temperature thermometers. Thus, measurements during the summer months for shallow depths may be overestimated, and record the near surface air temperature rather than the BHT of interest (Gray et al., 2012). However, our dataset contains only 7 BHTs lower than 40 °C which are all over 30 °C and that present no systematics with the month of the measurement, suggesting that no seasonal effect biases our data.

In order to test the hypotheses (4) and (5) we have computed the theoretical 1D conductive equilibrium temperatures for all the wells we have used (Fig. 13, Supplementary material). We used available thermal conductivities measured in the area of Neuchâtel (Table 1) with assigned 15% uncertainties, a basal heat flux of 73 mW/m² ($\pm 10\%$) as calculated, and a surface temperature of 10 °C.

Table 1

Thermal conductivities used to compute the conductive thermal profiles in Fig. 13 and Supplementary Material (adapted from CREGE, 2012).

Formation	Thermal Conductivity (W/m/K)
Superficial	2.0 \pm 15%
Molasse	2.2 \pm 15%
Eocene	2.5 \pm 15%
Lower Cretaceous	3 \pm 15%
Upper Jurassic	2.9 \pm 15%
Middle Jurassic	2.6 \pm 15%
Lower Jurassic	2 \pm 15%
Trias	2.9 \pm 15%
Permo-Carboniferous	2.9 \pm 15%

The temperature solutions were calculated using the GeoTemp™ software (Ricard and Chanu, 2013).

Results show that, below 1000 m depth, temperature profiles calculated with this conductive model overlap within uncertainties with temperatures obtained with the geostatistical model (Fig. 13, Supplementary data). In turn, above 1000 m depth, corrected temperature data and the geostatistical model tend to return temperatures that are significantly warmer than the purely conductive model for 9 wells (Treyvagnes, Eclépens, Savigny, Humilly_2, Savoie_109, Savoie_107, La Taille_1D, Chevalley and Reine Hortense; Fig. 13, Supplementary data). While thermal blanketing caused by a hypothetical shallow low conductivity layer could provide an explanation for the high temperatures and the low thermal gradient below this layer, the distinct geology of these anomalously warm wells cannot account for the high temperatures recorded above 1000 m depth. Therefore, hypothesis (4) is unlikely to fully explain these temperatures.

The remaining possibility is that many of our data for the shallowest 2000 m have been collected from places affected by upwelling of hot fluids from depth, most likely through fractures.

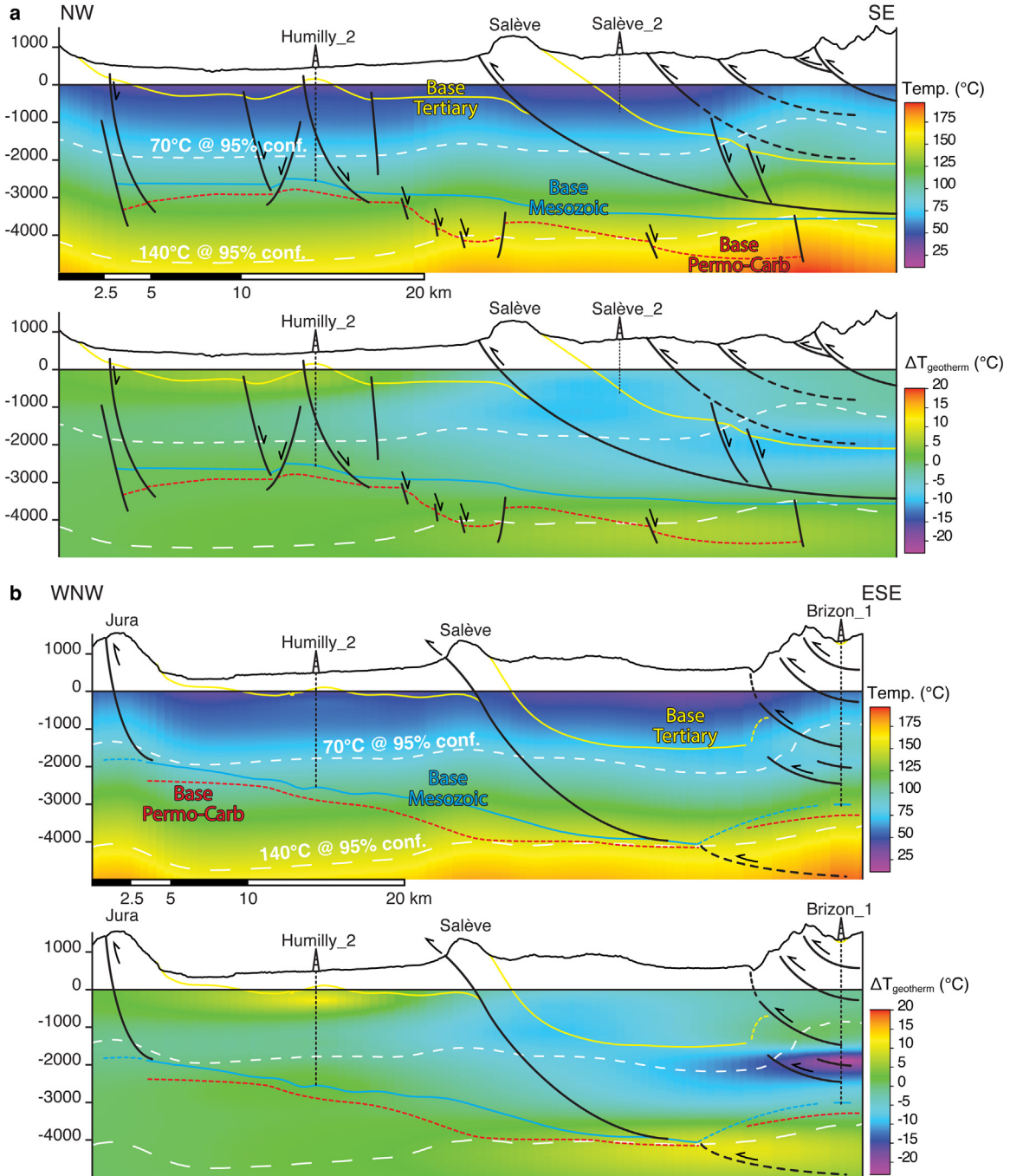


Fig. 10. NW-SE and W-E cross sections in the 3D model for the Geneva area. The exact location of the section is shown on Figs. 1 and 8. Geological interpretation are from Gorin et al. (1993) and Sommaruga et al. (2012).

Such resurgence zones are indeed known at several locations along the foothill of the Jura (Fig. 1; Yverdon-les-Bains, Aix-les-Bains, Moiry; Muralt, 1999) and along the Salève ridge (Fig. 1; Etrembière, La Caille, Bromines, Poisy, Lovagny; Bonvoisin, 1786; Moret, 1939). The comparison between the geostatistical and the conductive models for the first 2000 m depth suggests that heat advection is happening at the 9 anomalously warm wells listed above. Interestingly, all of them are located within 1 km of a major fault zone and/or crosscut a fault in their first 2000 m (Fig. 1). In contrast, many wells for which we observe a good agreement (within uncertainty) between the conductive and the geostatistical models are located further away from these major faults. This shows that, at least in their shallowest part (>2000 m depth), where the

uncertainties of the conductive model are the lowest, the temperature profile of most wells can be explained by conductive heat exchange using the thermal conductivities of Table 1. This analysis suggests that hypothesis (5) may be the main explanation for both the high thermicity and the low thermal gradient of the shallow WAMB. This, however, does not exclude minor additional contributions arising from inaccurate BHT corrections or locally lower thermal conductivities of the formations.

6.2. Identification of thermal anomalies

Several thermal anomalies are identified in the geostatistical model we have constructed (Figs. 8–11). They represent positive or

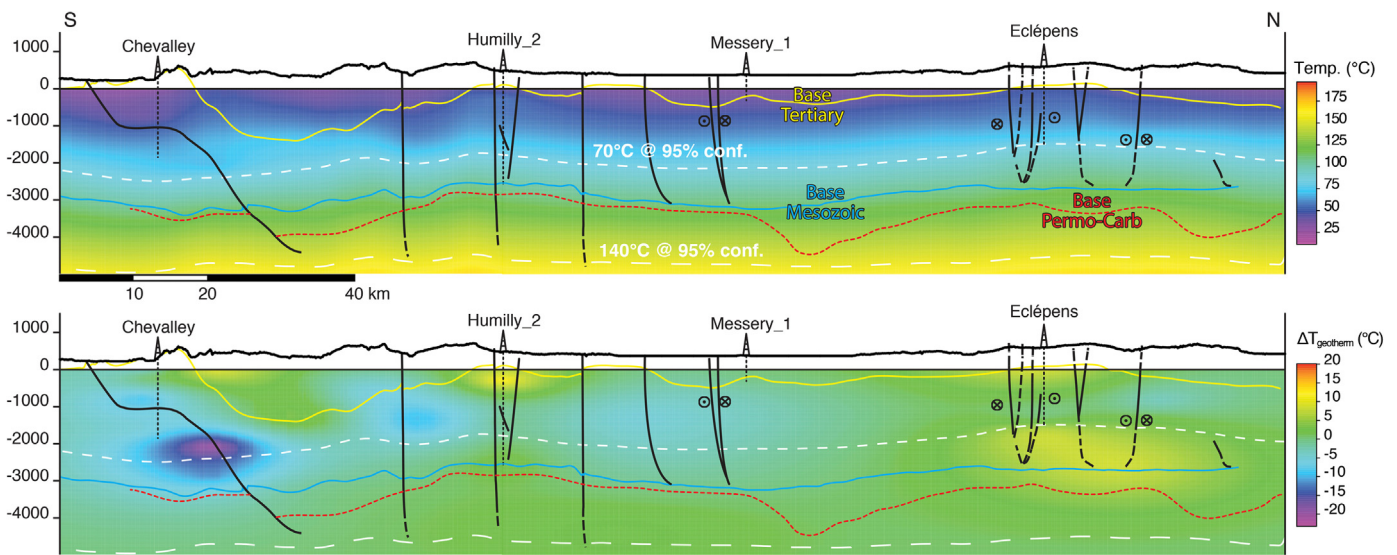


Fig. 11. NE-SW cross section in the 3D model for the WAMB. The exact location of the section is shown on Figs. 1 and 8. Geological interpretation are taken from the GeoMol 3D model (www.geneve.geomol.ch) and Sommaruga et al. (2012).

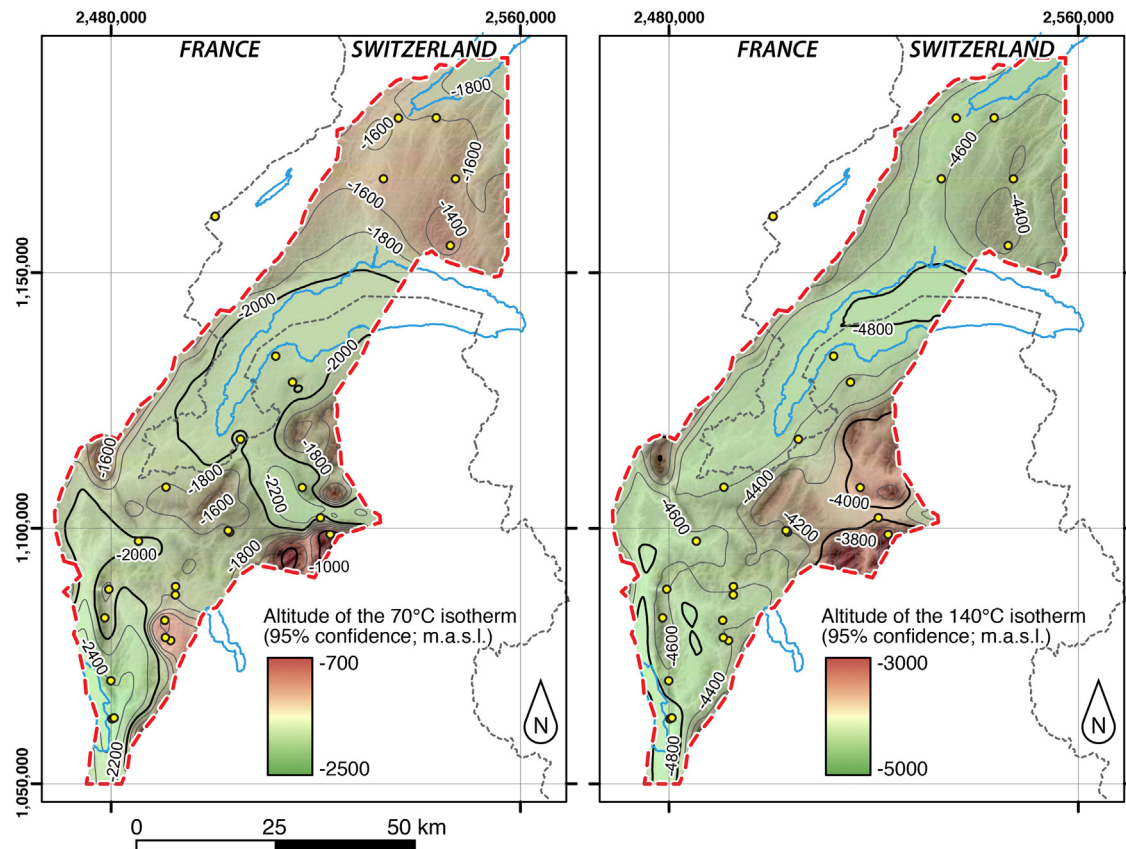


Fig. 12. Elevation maps of the 70 °C and 140 °C isotherms at 95% confidence according to the geostatistical 3D model wrapped on the surface topography.

negative deviations from the geothermal background field used to build the model (i.e. $T_{geotherm}(\text{°C}) = 25.4 z(\text{km}) + 23.2$). Areas close to known geothermal springs often show positive temperature anomalies of >10 °C. Furthermore, close to data points, where the residual temperatures are the most variable (a logical result of the interpolation) the standard error (1σ) is around 4 °C (Fig. 13). Thus anomalies of >10 °C represent statistically significant deviations away from the fitting geotherm (at $>95\%$ confidence). Thus defined, a number of both positive and negative thermal anomalies

can be identified across the WAMB. From north to south, positive (hot) anomalies are located south of Yverdon-les-bains, at shallow depth (ca. -200 m.a.s.l.) around the Humilly_2 well, at great depth (ca. -4000 m.a.s.l.) below the subalpine Molasse SE of Geneva (Borne plateau), in the southern part of the Salève ridge and at shallow depth north of Aix-les-Bains. In addition, two prominent negative (cold) anomalies can be identified at depth along the prealpine-subalpine front (SE of Geneva) and below the N-S Chambotte ridge.

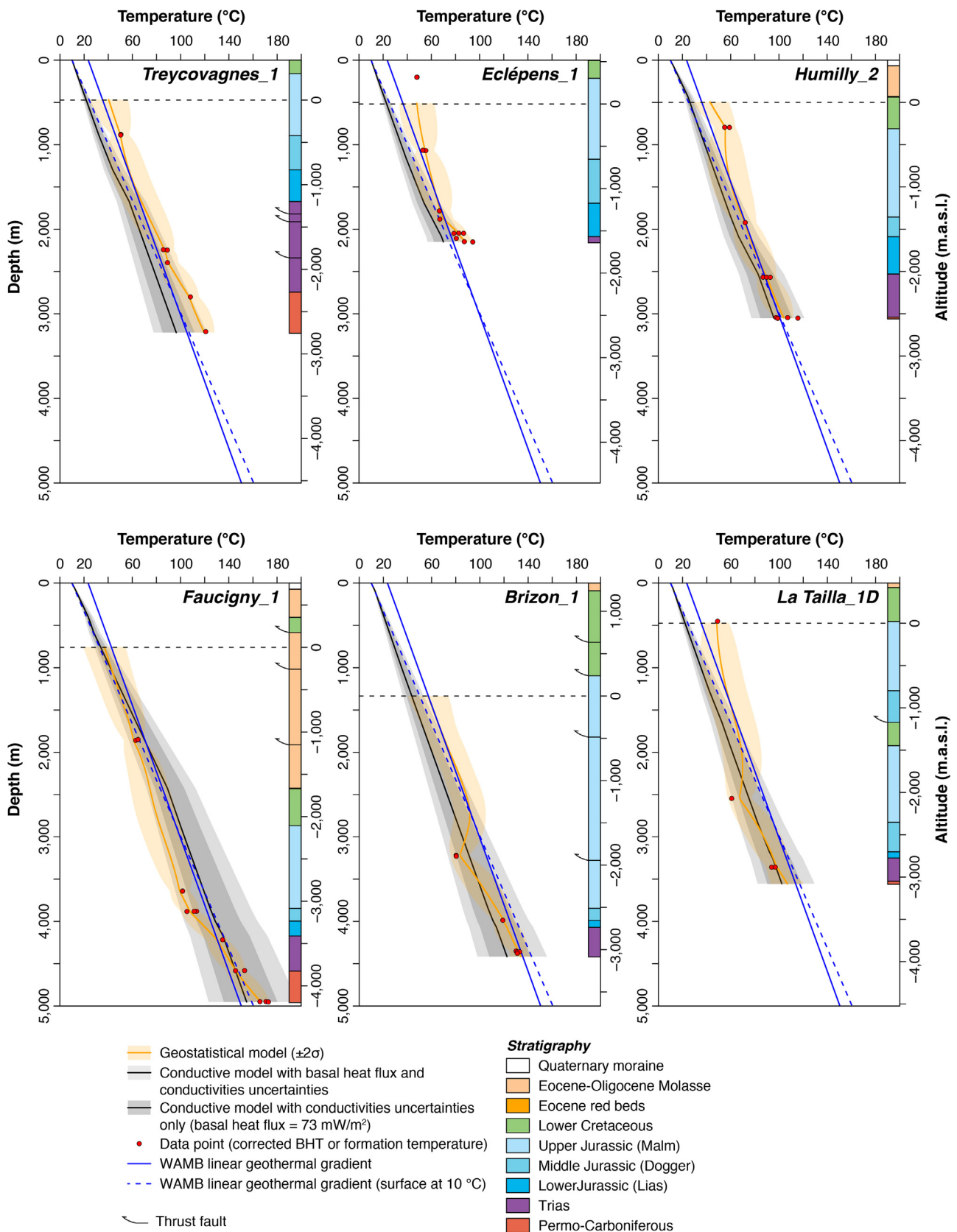


Fig. 13. Comparison between temperature data (corrected if BHT), the geostatistical thermal model and the conductive thermal model for select wells.

Based on the comparison between the geostatistical and conductive thermal profiles along the wells (Fig. 13, Supplementary Material), it appears that these anomalies are unlikely to be

explained by purely conductive heat exchange. Indeed, for a given basal heat flux, the uncertainty of our 1D conductive thermal profiles (Fig. 13) can hardly explain the identified temperature

anomalies and the evolution of the local geothermal gradients with depth. Localized anomalies similar to those we observe would require unrealistic conductivity contrasts between rock units to be caused by conductive heat refraction alone. Therefore, some amount of advective heat transport through fluid circulation should occur. Several studies which have modelled the thermal response of rock formations to fluid circulation (Bredehoeft and Papaopoulos, 1965; Lu and Ge, 1996; Ziegler and Blackwell, 1986) make the basis of our interpretation of the thermal anomalies identified in the WAMB. Below, we discuss the possible causes of the identified thermal anomalies in the light of available geological, geochemical and hydrological data.

6.3. Anomalies of the Yverdon area

Our geostatistical model suggests that a large area south of Yverdon has overall slightly higher temperatures by a few degrees compared to the average WAMB. This is particularly well shown on Fig. 12 where the 70 °C isotherm at 95% confidence rises over −1600 m.a.s.l., compared to around −2000 m.a.s.l. for the southern part of the WAMB (the density of measurement and the average temperature uncertainty is similar in both areas). A positive thermal anomaly with temperatures of 70–100 °C is located in the area of the Eclépens well at −1600 to −2800 m.a.s.l. close to the base of the Mesozoic units and extends toward Treycovagnes (Figs. 9 and 11). A second anomaly is present at shallower depth (around 0 m.a.s.l.) around the Eclépens well and has temperatures around 50 °C (Figs. 8, 9 and 11).

This region is characterized by intense faulting between two subvertical NW-SE dextral wrench faults: the Vallorbe-Mormont-Eclépens fault system to the south (next to the Eclépens well) and the Piéchat-Chamblon-Chevressy fault system (next to Yverdon) to the north (Fig. 1). Several N-S striking wrench faults occur within this block (Fig. 1). Interestingly, the Piéchat-Chamblon-Chevressy fault system is directly associated with the thermal system exploited at Yverdon (not included in this study, Muralt et al., 1997). Based on geochemical, isotopic and hydrologic evidences Muralt (1999) shows that the hydrologic system at Yverdon is mostly made of a shallow artesian aquifer in the Upper Jurassic (Malm) sediments and a deeper one possibly in the Middle Jurassic (Dogger) sediments (at least above the Triassic), both recharged through karsts in the adjacent Jura Haute Chaîne. An average residence time of >1 ka has also been estimated, which provide ample time for the water to reach thermal equilibrium with the rock formations (Muralt, 1999).

Using gravimetric and geological data combined with modelling, Altwegg (2015) showed that in the area of Eclépens, known faults exhibit a distinct negative gravimetric anomaly, which is interpreted in terms of highly damaged zone with an associated high bulk porosity. This together with our temperature model indicate that at least the shallow thermal anomaly at Eclépens is due to fluid circulation and associated advective heat transport along the highly permeable fault zone. This thermal system is probably very similar to the one present at Yverdon. However, it does not provide an explanation for the deeper thermal anomaly and the generally high-level 70 °C isotherm in this region.

Using gravimetric and geologic data Altwegg (2015) suggested that a thick (>3 km) Permo-Carboniferous trough should be present in the northern part of the WAMB around Yverdon. Nearly 500 m of such sediments have been intercepted by the Treycovagnes well and are under abnormally high temperatures (Fig. 13). Furthermore, the geothermal gradient in the Eclépens well suddenly increases in the Triassic sediments to >50 °C/km (Fig. 13). These features can readily be explained by an insulated fluid convection cell capped by impermeable Triassic sediments. Under this hypothesis, hot water may rise through fractures in the crystalline

basement and are collected in permeable Permo-Carboniferous and/or Lower Triassic sediments (permeable sandstones) where they release their heat. Subsequently, conductive heat transport dominates in the overlying impermeable sediments (which are consequently affected by a high thermal gradient). This configuration is strikingly analogous to the one present at the Soultz geothermal field (Rhine graben, France/Germany) where insulated convective cells are restricted to the basement and the Lower Triassic sandstones (Vidal et al., 2015).

6.4. Anomalies of the prealpine-subalpine front

The prealpine-subalpine front exhibits a spectacular negative thermal anomaly (of ca. −20 °C) at around −2000 to −3000 m.a.s.l. that has been intersected in the Upper to Middle Jurassic units (Malm and Dogger) in the Brizon and Fauchigny wells (Figs. 8, 10 and 13). This anomaly appears to connect upward and westward to the Salève ridge, though with a lower magnitude of ca. −10 °C (Fig. 10). These features may suggest that meteoric waters collected in the important karstic network of the Salève (Conrad and Ducloz, 1977; Martini, 1962) are channeled in the Cretaceous and/or Jurassic formations toward the Alps and result in a net cooling of the rocks. The important magnitude of the cooling over the >20 km distance from the suspected recharge area suggests that the residence time of the waters may be rapid and consequently that the water flux may be important. This is most likely achievable if we consider a well-developed karstic network in the Cretaceous and/or Jurassic formations.

In the Fauchigny well, the cold anomaly in the Jurassic units ramps up into a hot anomaly as it enters the Permo-Carboniferous units (Fig. 13). This results in a well-defined geothermal gradient of ca. 55 °C/km from 4000 to 5000 m depth that cannot be explained by a purely conductive heat transport regime (Fig. 13). Although the upper part of this high gradient zone may result from the cold anomaly on top, the high temperatures recorded in the Permo-Carboniferous rocks suggest that this high gradient probably marks the top of an insulated convective cell in the Permo-Carboniferous basement. In a similar way to the deep anomaly south of Yverdon (see above), the Triassic sediments may act as impermeable layers confining fluid circulation to deeper levels. This is again possibly analogous to the fractured basement confined convective cells of the Soultz geothermal field (Vidal et al., 2015).

6.5. Anomalies of the Geneva basin and the Salève ridge

South of Geneva, a positive thermal anomaly is recorded in the Humilly 2 well at ca. −200 m.a.s.l. (Figs. 8, 10, 11 and 13). This anomaly appears to pinpoint upward fluid circulation. The Humilly 2 well has actually been drilled within one of the wrench fault zone that transects the Geneva basin (Gorin et al., 1993) suggesting that fluid convection is most likely promoted by intense fracturation of the rocks.

Surprisingly, our model does not show any temperature anomaly associated with the most active wrench fault of the Geneva basin along the Vuache ridge (Figs. 8 and 11). This may be explained by the lack of significant data as depicted by the large kriging variance in this area (mostly >8 °C). Indeed, only two temperature data at around −1400 and −1600 m.a.s.l. in the Middle Jurassic are available in the Musiège well, drilled on the southernmost termination of the Vuache ridge (Fig. 1). Nevertheless, historical archives shed some light on the existence of hydrothermal systems associated with the Vuache fault: on November 14th, 1840 the temperature of the air suddenly increased within the Fort l'Ecluse (A military fort built on a cliff at the intersection of the Rhône river and the Vuache fault), and the atmosphere there was described as "suffocating" (La Phalange, 1840; Perrey, 1845). It was associated with a dull sound

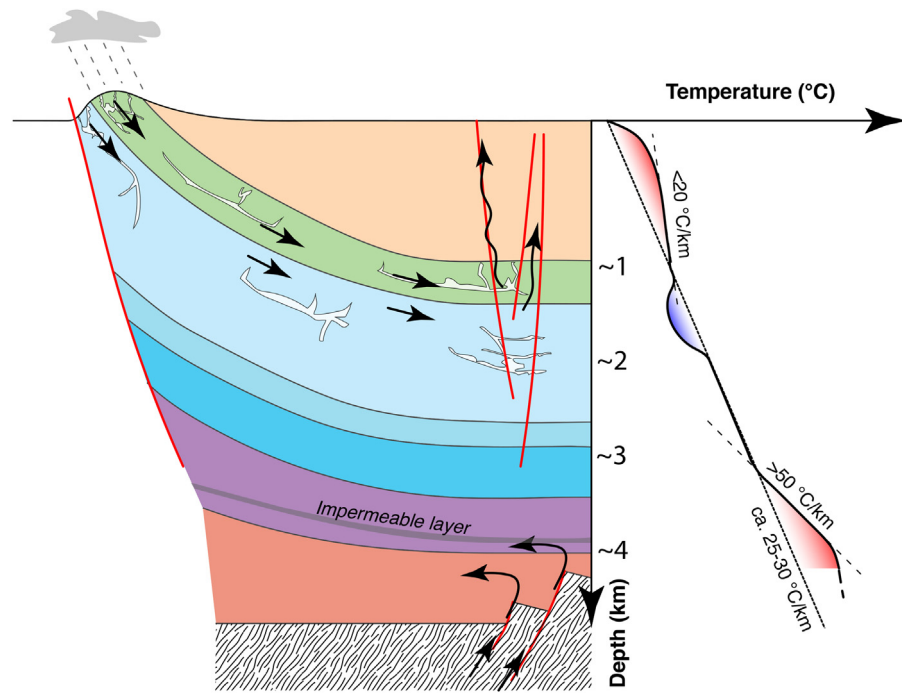


Fig. 14. Typology of the thermal anomalies identified in the WAMB. Approximate depth is shown for reference but may strongly vary from one place to another.

coming from underground and left a sulfurous smell within the fort. It is reported that twice the Major was about to order the evacuation of the fort, before everything came back to normal. More recently, an $M_L 5.2$ ($M_W 4.8$; Dufumier, 2002) earthquake on July 15th, 1996 on the southern part of the Vuache fault caused nearby thermal sulfurous springs (e.g. Bromines) to change their flow for few months (Thouvenot et al., 1998). This shows that the Vuache fault zone is (at least locally) affected by active hydrothermal system.

At the southern tip of the Salève ridge, the Savoie_101 and Savoie_104 wells define a positive thermal anomaly at -500 to -1500 m.a.s.l. in close proximity to known resurgences of thermal waters on surface (Figs. 1 and 8). This causes the 70°C isotherm at 95% confidence to rise above -1400 m.a.s.l. (Fig. 12). This anomaly is likely to be due to fluid circulation in fractures related to the complex faulting of the southern tip of the Salève mountain.

6.6. Anomalies of Aix-les-Bains and the Chambotte ridge

Both a deep (-500 to -2000 m.a.s.l.) cold and a shallow (ca. 0 m.a.s.l.) hot anomaly are observed along the Chambotte ridge and at Aix-les-Bains (Figs. 8 and 11). The presence of thermal water springs in the area of Aix-les-Bains proves that vertical fluid advection is the main mechanism causing the shallow positive thermal anomaly in this area. However, the origin of these waters is complex to determine. Indeed, detailed hydrologic and geochemical tracing of the thermal and subthermal springs of Aix-les-Bains has revealed that they result from the mixing of 3–4 water components (Muralt, 1999). Among these components, the two main contributors are probably one of deep origin recharged in Lower-Cretaceous to Upper Jurassic karst systems in the Jura west of Aix-les-Bains mixed with one of shallower origin recharged in the Chambotte ridge and flowing from north to south (Muralt, 1999). The deep component reaches depth in excess of 1500 m in a captive aquifer, and the water rises up through fractures and thrust faults in the anticlinal Chambotte ridge. The lateral circulation of the waters is likely the main reason for the negative thermal anomaly at this depth. Considering pulsed infiltration and fluid circulation stages

in between the Quaternary glaciations Gallino et al. (2009) could reproduce today's deep thermal field of the Aix-les-Bains area.

7. Geothermal potential of the WAMB

In this study we aim at exploiting available temperature data from hydrocarbon and geothermal campaigns from the 1930s to the 1990s. A geostatistical treatment of these data using a kriging interpolator allows us to define the thermal state of the WAMB and to identify areas where fluid circulation (lateral, downward or upward) may be the principal cause of disruption of the steady state background geothermal field and causes heat advection.

We show that the WAMB has an overall lower geothermal gradient than expected of 25 – 30 $^\circ\text{C}/\text{km}$ (Fig. 5). Nevertheless, many areas of enhanced thermal regime could be located in the study area. We interpret them to relate principally to upward fluid circulation through fractures perhaps together with a contribution from local conductive heat refraction. We could recognize two types of such convection cells. The first one is related to aquifers in Jurassic to Lower Cretaceous rocks where artesian hydraulic gradient cause upward fluid circulation in fractured rocks along mapped fault corridors (Fig. 14). This usually results in shallow temperature anomalies located in the first 2000 m below surface and to locally low geothermal gradient of ca. 20 $^\circ\text{C}/\text{km}$. The second type of positive thermal anomaly appears to be located in some places within the basal Permo-Carboniferous to Lower Triassic sediments (Bundsandstein; Fig. 14). Indeed, when compared to the other stratigraphic units of the WAMB, Permo-carboniferous sediments are the only one to record median temperature more than 10 $^\circ\text{C}$ higher than the average thermal gradient of the basin (Fig. 6b). Furthermore, in few wells (e.g. Eclépens, Faugny), the high thermal gradient of >50 $^\circ\text{C}/\text{km}$ in the Triassic sediments likely indicates that water convection is occurring below this level. Using independent constrains, Mazurek et al. (2006) also suggest that modern fluid circulation might have taken place along Paleozoic basement faults, and has possibly been triggered by loading-unloading cycles due to the Quaternary glaciations. Few cold temperature anomalies have also been identified mainly along the prealpine-subalpine

front and the Chambotte ridge to the south of the basin. They appear to be related to artesian fluid circulation in well-developed karstic aquifers of the Upper Jurassic to Lower Cretaceous formations recharged on the Jura Haute Chaine or related to inlier ridges within the basin (e.g. Salève, Chambotte; Fig. 14).

The present study highlights that the WAMB has a geothermal potential for both direct use and electricity production, confirming earlier estimates (Baujard et al., 2007). Exploration for direct use geothermal resource should hence focus on faulted and karstic reservoir that appear to be present in many locations across the basin. Although the karstic reservoirs may display negative thermal anomalies (10–20 °C below average), it could readily be compensated by their potentially important volume and important water flow as suggested by this study. Electricity production may be envisioned in Permo-Carboniferous troughs where the 140 °C isotherm lies above the crystalline Variscan basement and where hot fluids probably rise from basement-rooted faults. Preliminary measurements on Permo-Carboniferous to Lower Triassic siliciclastic sediments frequently yield values above 1 mD (E. Rusilon, ongoing work) and suggest that such formations may constitute an interesting target. However, determining the exact location, boundaries and thickness of the Permo-Carboniferous troughs in the WAMB remains very challenging due to the relatively low-resolution deep seismic signal and the often similarity in seismic response to the crystalline basement (Gorin et al., 1993). Using gravimetric and geological constrains, Altwegg (2015) suggests that the largest troughs are located south of Yverdon and SE of Geneva mainly below the Salève ridge and the Subalpine Molasse. This seems to be confirmed by few seismic based cross sections in this area (Gorin et al., 1993) and deep wells (Figs. 9–11). Further gravity forward modeling in the WAMB is likely to provide improved characterization of the geometry of the Permo-Carboniferous trough and of the most significant structures with high fracture porosity (e.g., Abdelfettah et al., 2014; Altwegg et al., 2015). Although not considered in the present study, preliminary works indicate that the top of the (altered) crystalline basement may host an additional important geothermal potential compatible with electricity production owing to its high temperatures across the WAMB (Baujard et al., 2007).

8. Concluding remarks

The present study is essentially based on hydrocarbon exploration data earlier than 1990s. At that time oil and gas exploration was designed for conventional reservoirs defined by their primary porosity while intensely fractured zones tended to be avoided. The approach used in this study provides an easy-to-implement and efficient way to reveal zones of thermal anomaly in sedimentary basins. Furthermore, although the geostatistical description of the dataset and the kriging interpolation has the great advantage to propagate the uncertainties while honoring the data, it also has a tendency to smooth the interpolated variable. The consequences of both of these features are that (1) significantly more thermal anomalies may be present in the WAMB in areas that have not been drilled (e.g., between Geneva and Lausanne where important faults with enhanced hydraulic conductivity are recognized but no temperature data is available; Baujard et al., 2007), and (2) that many anomalies may be of much greater magnitude than those identified in the present study. More temperature data in the WAMB could obviously lead to a more accurate and more precise thermal model of the basin. Keeping in mind that positive or negative thermal anomalies pinpoint the presence of fluid convection, the great geothermal potential of the WAMB for low-enthalpy resources makes little doubt. Furthermore, water reservoirs in the primary rock porosity (see Fig. 2) with minimal fluid circulation that

could not be identified in the present study (no thermal anomaly) would add to the resource potential of the WAMB. This preliminary assessment of the thermal state and geothermal potential of the WAMB should not hide the need for a more accurate understanding of the subsurface geological and of petrophysical characteristics and heterogeneity in order to develop a proper uncertainty and risk management strategy that would guarantee the success of the ongoing exploration projects. In particular, improving our knowledge of the 3D architecture of the basin and the variability of the thermal conductivities, porosity and permeability of the formations within the 3D domain will allow rigorous 3D conductive heat flow modelling and/or groundwater flow modelling.

Acknowledgments

This project was funded by the Swiss federal research program SCER-SoE (KTI 2013.0288) and benefited from inputs from the EC Interreg GeolMol project and the exploration program “GEothermie 2020” promoted by the Services Industriels de Genève and State of Geneva. We also acknowledge three anonymous reviewers for their constructive comments.

Appendix A. Supplementary data

Supplementary data associated with this article can be found, in the online version, at <http://dx.doi.org/10.1016/j.geothermics.2017.01.004>.

References

- Abdelfettah, Y., Schill, E., Kuhn, P., 2014. Characterization of geothermally relevant structures at the top of crystalline basement in Switzerland by filters and gravity forward modelling. *Geophys. J. Int.* 199, 226–241, <http://dx.doi.org/10.1093/gji/ggu255>.
- Agemar, T., Schellschmidt, R., Schulz, R., 2012. Subsurface temperature distribution in Germany. *Geothermics* 44, 65–77, <http://dx.doi.org/10.1016/j.geothermics.2012.07.002>.
- Allen, P.A., Allen, J.R., 2013. *Basin Analysis*. Wiley-Blackwell, <http://dx.doi.org/10.2113/gsecongeo.101.6.1314>.
- Altwegg, P., Schill, E., Abdelfettah, Y., Radogna, P.-V., Mauri, G., 2015. Toward fracture porosity assessment by gravity forward modeling for geothermal exploration (Sankt Gallen, Switzerland). *Geothermics* 57, 26–38, <http://dx.doi.org/10.1016/j.geothermics.2015.05.006>.
- Altwegg, P., 2015. *Gravimetry for Geothermal Exploration. Methodology, Computer Programs and Two Case Studies in the Swiss Molasse Basin*. Université de Neuchâtel (PhD thesis).
- Andaverde, J., Verma, S.P., 2005. Uncertainty estimates of static formation temperatures in boreholes and evaluation of regression models. *Geophys. J. Int.* 160, 1112–1122, <http://dx.doi.org/10.1111/j.1365-246X.2005.02543.x>.
- Baujard, C., Signorelli, S., Kohl, T., 2007. *Atlas des ressources géothermiques de la Suisse occidentale: domaine Sud-Ouest du Plateau Suisse*, vol. 40. Commission Suisse de Géophysique, 56 p.
- Bertani, R., 2012. Geothermal power generation in the world 2005–2010 update report. *Geothermics* 41, 1–29, <http://dx.doi.org/10.1016/j.geothermics.2011.10.001>.
- Bonte, D., Guillou-Frottier, L., Garibaldi, C., Bourgine, B., Lopez, S., Bouchot, V., Lucazeau, F., 2010. Subsurface temperature maps in French sedimentary basins: new data compilation and interpolation. *Bull. Soc. Geol. Fr.* 181, 377–390, <http://dx.doi.org/10.2113/gssgbull.181.4.377>.
- Bonvoisin, D., 1786. *Analyse des principales eaux de la Savoie. Mémoires de l'Académie Royale des Sciences de Turin Seconde partie*, 419–454.
- Bredehoef, J.D., Papaopoulos, I.S., 1965. Rates of vertical groundwater movement estimated from the Earth's thermal profile. *Water Resour. Res.* 1, 325–328, <http://dx.doi.org/10.1029/WR001i002p00325>.
- CREGE, 2012. Programme GeoNE – Développement de la géothermie profonde dans le canton de Neuchâtel. Rapport final de la Phase 1. Rapport CREGE 12-02, 254 p.
- Cederbom, C.E., Sinclair, H.D., Schlunegger, F., Rahn, M.K., 2004. Climate-induced rebound and exhumation of the European Alps. *Geology* 32, 709–712, <http://dx.doi.org/10.1130/G20491.1>.
- Cederbom, C.E., van der Beek, P., Schlunegger, F., Sinclair, H.D., Oncken, O., 2011. Rapid extensive erosion of the North Alpine foreland basin at 5–4 Ma. *Basin Res.* 23, 528–550, <http://dx.doi.org/10.1111/j.1365-2117.2011.00501.x>.
- Charollais, J., Weidmann, M., Berger, J.-P., Engesser, B., Hotellier, J.-F., Gorin, G., Reichenbacher, B., Schäfer, P., 2007. *The Molasse in the Greater Geneva area and its substratum. Archives des Sciences. Société de Physique et d'Histoire Naturelle de Genève* 60, 59–173.

- Chevalier, G., Diamond, L.W., Leu, W., 2010. Potential for deep geological sequestration of CO₂ in Switzerland: a first appraisal. *Swiss J. Geosci.* 103, 427–455, <http://dx.doi.org/10.1007/s00015-010-0030-4>.
- Chiles, J.-P., Delfiner, P., 2012. *Geostatistics: Modeling Spatial Uncertainty*, second edition. John Wiley & Sons, Inc., Hoboken, NJ, USA, <http://dx.doi.org/10.1002/9781118136188>.
- Cohen, K.M., Finney, S.C., Gibbard, P.L., Fan, J.X., 2013. *The ICS international chronostratigraphic chart*. *Episodes* 36, 199–204.
- Conrad, M.A., Ducluz, C., 1977. *Nouvelles observations sur l'Urgonien et le Sidérolithique du Salève*. *Eclogae Geol. Helv.* 70, 127–141.
- Davis, R.W., 2012. Deriving geothermal parameters from bottom-hole temperatures in Wyoming. *AAPG Bull.* 96, 1579–1592, <http://dx.doi.org/10.13061/11081110167>.
- Deming, D., 1989. Application of bottom-hole temperature corrections in geothermal studies. *Geothermics* 18, 775–786, [http://dx.doi.org/10.1016/0375-6505\(89\)90106-5](http://dx.doi.org/10.1016/0375-6505(89)90106-5).
- DiPippo, R., 2004. Second Law assessment of binary plants generating power from low-temperature geothermal fluids. *Geothermics* 33, 565–586, <http://dx.doi.org/10.1016/j.geothermics.2003.10.003>.
- Dowdle, W.L., Cobb, W.M., 1975. Static formation temperature from well logs – an empirical method. *J. Petrol. Technol.* 27, 1326–1330, <http://dx.doi.org/10.2118/5036-PA>.
- Dufumier, H., 2002. Synthesis of magnitude and focal mechanism computations for the M ≥ 4.5 earthquakes in France for the period 1995–2000. *J. Seismol.* 6, 163–181, <http://dx.doi.org/10.1023/A:1015606311206>.
- Forster, A., Merriam, D.F., 1995. A bottom-hole temperature analysis in the American Midcontinent (Kansas): implications to the applicability of BHTs in geothermal studies. In: Presented at the World Geothermal Congress, Florence, Italy, pp. 777–782.
- Forster, A., Merriam, D.F., Davis, J.C., 1997. Spatial analysis of temperature (BHT/DST) data and consequences for heat-flow determination in sedimentary basins. *Geol. Rundsch.* 86, 252–261, <http://dx.doi.org/10.1007/s005310050138>.
- Forster, A., 2001. Analysis of borehole temperature data in the Northeast German Basin: continuous logs versus bottom-hole temperatures. *Pet. Geosci.* 7, 241–254, <http://dx.doi.org/10.1144/petgeo.7.3.241>.
- Gallino, S., Josnin, J.-Y., Dzikowski, M., Cornaton, F., Gasquet, D., 2009. The influence of paleoclimatic events on the functioning of an alpine thermal system (France): the contribution of hydrodynamic-thermal modeling. *Hydrol. J.* 17, 1887–1900, <http://dx.doi.org/10.1007/s10040-009-0510-7>.
- Garibaldi, C., Guillou-Frottier, L., Lardeaux, J.M., Bonte, D., Lopez, S., Bouchot, V., Ledru, P., 2010. Thermal anomalies and geological structures in the Provence basin: implications for hydrothermal circulations at depth. *Bull. Soc. Geol. Fr.* 181, 363–376, <http://dx.doi.org/10.2113/gssgbull.181.4.363>.
- GeoMol Team, 2015. Assessing subsurface potentials of the Alpine Foreland Basins for sustainable planning and use of natural resources–Project Report, geomol.eu. Augsburg, IfU.
- Goovaerts, P., 2000. Geostatistical approaches for incorporating elevation into the spatial interpolation of rainfall. *J. Hydrol.* 228, 113–129, [http://dx.doi.org/10.1016/S0022-1694\(00\)00144-X](http://dx.doi.org/10.1016/S0022-1694(00)00144-X).
- Gorin, G.E., Signer, C., Amberg, G., 1993. Structural configuration of the western Swiss Molasse Basin as defined by reflection seismic data. *Eclogae Geol. Helv.* 86, 693–716.
- Goutorbe, B., Lucazeau, F., Bonneville, A., 2007. Comparison of several BHT correction methods: a case study on an Australian data set. *Geophys. J. Int.* 170, 913–922, <http://dx.doi.org/10.1111/j.1365-246X.2007.03403.x>.
- Gray, D.A., Majorowicz, J., Unsworth, M., 2012. Investigation of the geothermal state of sedimentary basins using oil industry thermal data: case study from Northern Alberta exhibiting the need to systematically remove biased data. *J. Geophys. Eng.* 9, 534–548, <http://dx.doi.org/10.1088/1742-2132/9/5/534>.
- Guillou-Frottier, L., Carré, C., Bourgine, B., Bouchot, V., Genter, A., 2013. Structure of hydrothermal convection in the Upper Rhine Graben as inferred from corrected temperature data and basin-scale numerical models. *J. Volcanol. Geotherm. Res.* 256, 29–49, <http://dx.doi.org/10.1016/j.jvolgeores.2013.02.008>.
- Hagke, C., Cederbom, C.E., Oncken, O., Stöckli, D.F., Rahn, M.K., Schlunegger, F., 2012. Linking the northern Alps with their foreland: the latest exhumation history resolved by low-temperature thermochronology. *Tectonics* 31, <http://dx.doi.org/10.1029/2011TC003078>, n/a–n/a.
- Harrison, W.E., Luza, K.V., Prater, M.L., Cheung, P.K., 1983. *Geothermal Resource Assessment of Oklahoma*, vol. 3. Oklahoma Geological Survey, Special Publication, 42 p.
- Horner, D.R., 1951. Pressure build-up in wells. In: Presented at the 3rd World Petroleum Congress, 28 May–6 June, The Hague, the Netherlands, World Petroleum Congress, pp. 25–43.
- Jenny, J., Burri, J.P., Muralt, R., Pugin, A., Schegg, R., Ungemach, P., Vuataz, F.-D., Wernli, R., 1995. *Le forage géothermique de Thônen (Canton de Genève)* Aspects stratigraphiques, tectoniques, diagénétiques, géophysiques et hydrogéologiques. *Eclogae Geol. Helv.* 88, 365–396.
- Kuhlemann, J., Kempf, O., 2002. Post-Eocene evolution of the North Alpine Foreland Basin and its response to Alpine tectonics. *Sediment. Geol.* 152, 45–78, [http://dx.doi.org/10.1016/S0037-0738\(01\)00285-8](http://dx.doi.org/10.1016/S0037-0738(01)00285-8).
- La Phalange, 1840. Faits divers, 25 novembre 1840. La Phalange journal de la science sociale 37, 632–634.
- Lo Russo, S., Boffa, C., Civita, M.V., 2009. Low-enthalpy geothermal energy: an opportunity to meet increasing energy needs and reduce CO₂ and atmospheric pollutant emissions in Piemonte, Italy. *Geothermics* 38, 254–262, <http://dx.doi.org/10.1016/j.geothermics.2008.07.005>.
- Lu, N., Ge, S., 1996. Effect of horizontal heat and fluid flow on the vertical temperature distribution in a semiconfining layer. *Water Resour. Res.* 32, 1449–1453, <http://dx.doi.org/10.1029/95WR03095>.
- Lucazeau, F., Ben Dhia, H., 2011. Preliminary heat-flow density data from Tunisia and the Pelagian Sea. *Can. J. Earth Sci.* 26, 993–1000, <http://dx.doi.org/10.1139/e89-080>.
- Martini, J., 1962. Les phénomènes karstiques de la chaîne du Salève. *Les Boueux* 3–4, 15–20.
- Mazurek, M., Hurford, A.J., Leu, W., 2006. Unravelling the multi-stage burial history of the Swiss Molasse Basin: integration of apatite fission track, vitrinite reflectance and biomarker isomerisation analysis. *Basin Res.* 18, 27–50, <http://dx.doi.org/10.1111/j.1365-2117.2006.00286.x>.
- McCann, T., Pascal, C., Timmerman, M.J., Krzywiec, P., López-Gómez, J., Wetzel, L., Krawczyk, C.M., Rieke, H., Lamarche, J., 2006. Post-Variscan (end Carboniferous-Early Permian) basin evolution in Western and Central Europe. *Geological Society, London, Memoirs* 32, 355–388. 10.1144/GSL.MEM.2006.032.01.22.
- Medici, F., Rybach, L., 1995. *Geothermal Map of Switzerland 1995 (Heat Flow Density)*, vol. 30. Commission Suisse de géophysique, 36 p.
- Moret, L., 1939. Origine géologique des sources thermales d'Aix-les-Bains. *Les Études rhodaniennes* 15, 161–162, <http://dx.doi.org/10.3406/geoca.1939.6554>.
- Muralt, R., Vuataz, F., Schönborn, G., Sommaruga, A., Jenny, J., 1997. *Intégration des méthodes hydrochimiques géologiques et géophysiques pour la prospection d'une nouvelle ressource en eau thermale. Cas d'Yverdon-les-Bains, pied du Jura*. *Eclogae Geol. Helv.* 90, 179–197.
- Muralt, R., 1999. *Processus hydrogéologiques et hydrochimiques dans les circulations profondes des calcaires du Malm de l'arc jurassien (zones de Delémont, Yverdon-les-Bains, Moiry, Genève et Aix-les-Bains)*. Commission Géotechnique Suisse.
- Nielsen, S.B., Balling, N., Christiansen, H.S., 1990. Formation temperatures determined from stochastic inversion of borehole observations. *Geophys. J. Int.* 101, 581–590, <http://dx.doi.org/10.1111/j.1365-246X.1990.tb05572.x>.
- Olea, R.A., 1999. *Geostatistics for Engineers and Earth Scientists*. Springer, US, Boston MA, <http://dx.doi.org/10.1007/978-1-4615-5001-3>.
- PGG, 2011. Evaluation du potentiel géothermique du canton de Genève – Vol. 1: Rapport final. Service cantonal de l'énergie – Services industriels de Genève, Genève, 300 p.
- PGV, 2003. Evaluation du potentiel géothermique du canton de Vaud, Rapport final. Service de l'environnement et de l'énergie, Vaud, 171 p.
- Pasquale, V., Chiozzi, P., Gola, G., Verdoya, M., 2008. Depth-time correction of petroleum bottom-hole temperatures in the Po Plain, Italy. *Geophysics* 73, E187–E196, <http://dx.doi.org/10.1190/1.2976629>.
- Pasquale, V., Chiozzi, P., Verdoya, M., Gola, G., 2012. Heat flow in the Western Po Basin and the surrounding orogenic belts. *Geophys. J. Int.* 190, 8–22, <http://dx.doi.org/10.1111/j.1365-246X.2012.05486.x>.
- Perrey, A., 1845. *Mémoire sur les tremblements de terre ressentis dans le bassin du Rhône*. *An. Sc. Phys. Nat. Agri. et Indus. Tome 8*, 265–346.
- Pfiffner, O.A., 1986. *Evolution of the North Alpine Foreland Basin in the Central Alps, Foreland Basins*. Blackwell Publishing Ltd., Oxford, UK, <http://dx.doi.org/10.1002/9781444303810> (chapter 11).
- Rühaak, W., 2014. 3-D interpolation of subsurface temperature data with measurement error using kriging. *Environ. Earth Sci.* 73, 1893–1900, <http://dx.doi.org/10.1007/s12665-014-3554-5>.
- Ricard, L.P., Chanu, J.-B., 2013. *GeoTemp™ 1.0: A MATLAB-based program for the processing, interpretation and modelling of geological formation temperature measurements*. *Comput. Geosci.* 57, 197–207, <http://dx.doi.org/10.1016/j.cageo.2013.04.003>.
- Rybäck, L., 1992. *Geothermal potential of the Swiss Molasse Basin*. *Eclogae Geol. Helv.* 85, 733–744.
- SIG, 2011. *Valorisation du forage de Thônex et étude du potentiel géothermique* (Report No. SIG/SP/IPRO/6530/CNO). Geneva, Switzerland, 31 p.
- Sepúlveda, F., Rosenberg, M.D., Rowland, J.V., Simmons, S.F., 2012. Kriging predictions of drill-hole stratigraphy and temperature data from the Wairakei geothermal field, New Zealand: implications for conceptual modeling. *Geothermics* 42, 13–31, <http://dx.doi.org/10.1016/j.geothermics.2012.01.002>.
- Signer, C., Gorin, G.E., 1995. New geological observations between the Jura and the Alps in the Geneva area, as derived from reflection seismic data. *Eclogae Geol. Helv.* 88, 235–265, <http://dx.doi.org/10.5169/seals-167674>.
- Sommaruga, A., Eichenberger, U., Marillier, F., 2012. *Seismic Atlas of the Swiss Molasse Basin (No. 44)*. Matér. Géol. Suisse, Géophys. Swiss Geophysical Commission.
- Sommaruga, A., 1999. Décollement tectonics in the Jura forelandfold-and-thrust belt. *Mar. Petrol. Geol.* 16, 111–134, [http://dx.doi.org/10.1016/s0264-8172\(98\)00068-3](http://dx.doi.org/10.1016/s0264-8172(98)00068-3).
- Teng, Y., Koike, K., 2007. Three-dimensional imaging of a geothermal system using temperature and geological models derived from a well-log dataset. *Geothermics* 36, 518–538, <http://dx.doi.org/10.1016/j.geothermics.2007.07.006>.
- Thouvenot, F., Fréchet, J., Tapponnier, P., Thomas, J.-C., Le Brun, B., Ménard, G., Lacassin, R., Jenatton, L., Grasso, J.-R., Coutant, O., Paul, A., Hatzfeld, D., 1998. The ML 5.3 Epagny (French Alps) earthquake of 1996 July 15: a long-awaited event on the Vuache fault. *Geophys. J. Int.* 135, 876–892, <http://dx.doi.org/10.1046/j.1365-246X.1998.00662.x>.
- Vidal, J., Genter, A., Schmittbuhl, J., 2015. How do permeable fractures in the Triassic sediments of Northern Alsace characterize the top of hydrothermal

- convective cells? Evidence from Soultz geothermal boreholes (France). *Geothermal Energy* 3, 8, <http://dx.doi.org/10.1186/s40517-015-0026-4>.
- Willett, S.D., Schlunegger, F., 2010. The last phase of deposition in the Swiss Molasse Basin: from foredeep to negative-alpha basin. *Basin Res.* 22, 623–639, <http://dx.doi.org/10.1111/j.1365-2117.2009.00435.x>.
- Wilson, M., Neumann, E.R., Davies, G.R., Timmerman, M.J., Heeremans, M., Larsen, B.T., 2004. Permo-Carboniferous magmatism and rifting in Europe: introduction. *Geol. Soc. London, Special Publications* 223, 1–10. 10.1144/GSL.SP.2004.223.01.01.
- Wong-Loya, J.A., Andaverde, J.A., del Rio, J.A., 2015. Improved method for estimating static formation temperatures in geothermal and petroleum wells. *Geothermics* 57, 73–83, <http://dx.doi.org/10.1016/j.geothermics.2015.06.002>.
- Ziagos, J.P., Blackwell, D.D., 1986. A model for the transient temperature effects of horizontal fluid flow in geothermal systems. *J. Volcanol. Geotherm. Res.* 27, 371–397, [http://dx.doi.org/10.1016/0377-0273\(86\)90021-1](http://dx.doi.org/10.1016/0377-0273(86)90021-1).